IEEE Access
Multidisciplinary | Rapid Review | Open Access Journal

Received April 11, 2021, accepted June 4, 2021, date of publication June 11, 2021, date of current version June 21, 2021.

*Digital Object Identifier 10.1109/ACCESS.2021.3088150*

# Effects of Rotor-Rotor Interaction on the Wake Structure and Thrust Generation of a Quadrotor Unmanned Aerial Vehicle

**SEUNGCHEOL LEE[1], SEOKBONG CHAE[1], SEONG YONG WOO[1,2], JAESUNG JANG[1], AND JOOHA KIM[1]**

[1]Department of Mechanical Engineering, Ulsan National Institute of Science and Technology (UNIST), Ulsan 44919, South Korea
[2]Institute of Andong Smart Farm (IASF), Andong 36728, South Korea

Corresponding author: Jooha Kim (kimjooha@unist.ac.kr)

This work was supported in part by the Basic Science Research Program through the National Research Foundation of Korea (NRF) by the Ministry of Education under Grant NRF-2019R1F1A106406612, and in part by the Civil-Military Technology Cooperation Program under Grant 18-CM-AS-22.

**ABSTRACT** In this paper, the effects of rotor-rotor interaction on the wake structure and thrust generation of a quadrotor unmanned aerial vehicle (UAV) are experimentally investigated in the rotor tip Reynolds number range of 34000 – 54000. The interaction strength is manipulated by varying the number of rotating rotors and the normalized rotor separation distance. A stronger rotor-rotor interaction places the inner tip vortices between rotors closer to each other, forming an upflow region through vortex pairing and intensifying the turbulence intensity between rotors. To comprehensively evaluate the effect of interaction on the wake structure, we propose a modified Landgrebe's model that accurately describes the wake boundary of UAV, given the number of rotating rotors and the normalized rotor separation distance. The wake analysis based on the model shows that the stronger the rotor-rotor interaction, the less the wake contracts and the closer the *vena contracta* moves to the rotor-tip path plane. The momentum theory combined with the modified Landgrebe's model shows that the loss of axial momentum transfer due to the wake inclination is insufficient to account for the thrust loss caused by the rotor-rotor interaction. This paper shows that the shift of the inner tip vortex away from the rotational axis and the corresponding increase of induced axial velocity followed by a decrease in the local effective angle of attack is another important mechanism for the thrust loss.

**INDEX TERMS** Rotor-rotor interaction, thrust, unmanned aerial vehicles, wake.

## I. INTRODUCTION

Rotary-wing unmanned aerial vehicles (UAVs) have significant advantages over fixed-wing UAVs in terms of hovering ability, maneuverability, vertical take-off and landing (VTOL) ability, flexibility in size, versatility, and affordability. Based on these advantages, rotary-wing UAVs have a variety of applications, including air quality assessment, aerial photography, remote sensing, surveillance, disease control, film recording, and delivery service. The majority of rotary-wing UAVs have more than two rotors, and this type of UAVs is called multirotor UAVs. Multirotor UAVs are being more widely used than the UAVs with one or two rotors because they are mechanically simpler. For example, single- or double-rotor UAVs should be equipped with a swashplate and variable pitch rotor blades to change the flight mode (e.g., from hovering to forward flight) by cyclically controlling the rotor blade pitch angle while the blade is rotating. However, since multirotor UAVs can switch the flight mode by simply varying the rotational speed of each rotor, there is no need to control or change the rotor blade pitch angle. Thus, for multirotor UAVs, no swashplate and no variable pitch rotor blades are necessary, which allows greater mechanical simplicity. Due to the mechanical simplicity achieved using multiple rotors, multirotor UAVs are not only easy to operate and repair but are also low in cost.

The use of multiple rotors simplifies the mechanical structure and operation of UAVs as described above, but rather complicates the wake structure of multirotor UAVs by the flow interaction between rotors. As the interaction between the flow around rotors is mainly governed by the two parameters of the number of rotating rotors and the distance between

The associate editor coordinating the review of this manuscript and approving it for publication was Rosario Pecora.

rotors, previous studies have investigated the effect of these parameters on the rotor wake characteristics. The effect of the number of rotating rotors was examined by comparing the wake of a single isolated rotor with that of twin rotors [1] and with that of quadrotors [2]. Zhou *et al*. [1] experimentally observed that the wake of a single rotor was directed straight down the rotor along the rotational axis, whereas, for twin rotors, the two rotor wakes were pulled toward each other. Similar wake bending was also found in the numerical study by Lee and Lee [2], where four rotors were rotated. In the experiment by Zhou *et al*. [1], the velocity field in the crossflow plane was measured to be circular behind the single rotor, but it was distorted into a droplet shape for twin rotors due to the flow disturbance caused by the two rotor wakes in close proximity. Both for twin rotors [1] and quadrotors [2], it was observed that the tip vortices trailed from the rotor blade interacted severely and thus dissipated faster compared to the tip vortices shed from a single rotor. Regarding the effect of the distance between rotors, several researchers have found that a decrease in the rotor separation distance induces a stronger interaction between the rotor wakes, resulting in a more complex wake structure. For example, as the rotors were moved closer to each other for UAVs with two or more rotors, the wake flow of a rotor was observed to move radially toward the nearby rotor and thus to be more asymmetric about the rotational axis [1]–[5]. The numerical works by Yoon *et al*. [3] and Lee and Lee [2] showed that, for quadrotor UAVs, an upward flow is formed at the center of the four rotors and becomes more prominent as the rotor separation distance decreased. The faster destruction of tip vortices into small spots at lower rotor separation distances was also experimentally and numerically observed for twin rotors [6] and quadrotors [2], which led to the faster transition of a rotor wake into a turbulent wake. On the other hand, when the rotor separation distance was greater than one rotor diameter for a quadrotor UAV, the mutual rotor interaction was shown to have little effect on the wake structure [2].

Although the previous studies mentioned above have been of great help in understanding the rotor wake variations caused by the aerodynamic interaction between rotors, in-depth quantitative analysis and modeling of rotor wakes are still needed to improve the viability and mission ability of multirotor UAVs. Considering that the tip vortex is the strongest vortical structure in the wake of a rotor and thus has a dominant influence on the evolution of the rotor wake [7]–[9], a modeling study on the wake boundary defined as the trajectory of the tip vortex is a necessary first step in understanding the aerodynamics of multirotor UAVs. An accurate description and prediction of the wake boundary can be very useful in assessing the aerodynamic performance, such as rotor efficiency and blade loads, and noise characteristics resulting from blade-vortex interaction [10]–[12]. Moreover, the experimental data on the wake boundary is critically important in the development of prescribed wake models and in the validation of new rotor wake models [13]. The wake geometry including the tip vortex location (i.e., wake boundary) of multirotor UAVs also plays an important role in practical applications such as the placement of a sensor for atmospheric sampling [14]–[20] and the determination of the spatial distribution of spraying droplets for plant protection [21]–[24]. However, to the best of our knowledge, there have been no models which are designed to describe and predict the wake geometry of multirotor UAVs. Due to the absence of a wake geometry model for multirotor UAVs, the Landgrebe's model [7], a wake geometry model developed for a single helicopter rotor, has been instead used in the studies on multirotor UAVs [25]–[27]. Landgrebe [7] developed a generalized model to predict the location of tip vortex trailing from a model helicopter rotor for a wide range of blade designs and operating conditions (e.g., aspect ratio, blade twist, number of blades, and tip speed) by conducting systematic experiments, which was later referred to as the Landgrebe's model. Unfortunately, the Landgrebe's model [7] cannot describe the complex wake boundary of multiple rotors because it was developed to model the wake of a single helicopter rotor. Moreover, even in the absence of rotor-rotor wake interaction, the Landgrebe's model [7] was found to be inaccurate in predicting the wake boundary of a single UAV rotor, as noted by Hein and Chopra [25]. In the present study, therefore, we developed a model that predicts the wake boundary of a multirotor UAV in hovering mode, which is complicated by the mutual rotor interaction, as a function of the number of rotating rotors and the distance between rotors.

The aforementioned changes in the wake structure induced by the rotor-rotor interaction results in a loss of thrust coefficient ($C_T = T/\rho A V_{\text{tip}}^2$; where $T$ is the thrust force, $\rho$ is the density of air, $A$ is the rotor disk area, and $V_{\text{tip}}$ is the rotor tip speed) compared to a single isolated rotor, as demonstrated in the previous numerical [2]–[5] and experimental [1], [6] investigations. Although there have been attempts to explain the thrust loss in terms of the wake deflection caused by the flow interaction between rotors, the causal relationship between the wake deflection and the thrust loss still requires further clarification. Young and Derby [28] hypothesized that the thrust loss might be due to the skewness of the flow far upstream (called upstream far-wake in their study) of the rotors. They derived an analytical equation that predicts thrust loss based on the hypothesis, but the proposed equation overpredicted the thrust loss. Veismann and Gharib [29] argued that the thrust loss caused by the rotor-rotor interaction is proportional to the inclination angle of the downstream wake instead of that of the upstream one. However, the thrust loss predicted based on the inclination angle of the downstream wake was shown to underpredict the experimentally measured thrust loss. Shukla and Komerath [6] conjectured that the interaction between the rotor blade and the tip vortex of the adjacent rotor blade may be a reason for thrust loss. However, the detailed mechanism of how the blade-vortex interaction induces a loss in the thrust generated remains still unclear. This study aims to extend current understanding of the relationship between a change in the wake structure and

the corresponding thrust variation. For this purpose, we estimate the thrust loss caused by the wake inclination, based on the model developed in this paper, and describe a mechanism other than the wake inclination responsible for the thrust loss by measuring the velocity fields near the rotors using digital particle image velocimetry (DPIV).

The rest of paper is organized as follows. Section II describes the quadrotor UAV model used in this study. Section III provides the experimental setup for wake velocity and thrust measurements. The experimental results are given in Section IV. Concluding remarks will be given in Section V.

## II. QUADROTOR UAV MODEL

Fig. 1 shows the quadrotor UAV model used in the present experiments. This model consists of four rotors, four brushless DC motors, and an X-shaped frame on which the motors are installed (Fig. 1(a)). The X-shaped frame consists of four arms arranged at equal angular intervals of 90° around the center of the frame. The motors are designed to move along the arms so that the distance between the adjacent rotor tips ($s$ in Fig. 1(b)) can be varied as desired without changing the total mass of the UAV model. That is, the distance between the adjacent rotor tips increases as the motors are mounted closer to the end of the X-shaped frame (e.g., from Fig. 1(b) to Fig. 1(c)), and vice versa. Note that all four motors are always kept the same distance from the center of the frame. The normalized distance between the adjacent rotor tips (hereafter referred to as the normalized rotor separation distance), $s/R_r$, can be varied between 0.13 and 2.37, where $R_r$ (=38 mm) is the rotor radius. Zhou *et al*. [1] claimed that, for twin rotors, the effect of rotor-rotor interaction on thrust generation was negligible when $s/R_r$ was higher than 2. The upper limit of $s/R_r$ in the present study was chosen to be somewhat higher than this value. This is because, according to previous studies [2], [3], [30], [31], a stronger rotor-rotor interaction was expected for the quadrotors investigated in this study than twin rotors. The lower limit of $s/R_r$ was chosen to be lower than the minimum $s/R_r$ considered in previous studies (e.g., 0.2 for Yoon *et al*. [3] and 0.4 for Lee and Lee [2]) on quadrotors so that more pronounced changes in wake structure, such as wake distortion and tip vortex breakdown, could be detected in this study. To avoid flow interference such as pressure fluctuations and tip-vortex breakdown caused by cylindrical arms located downstream of the rotors [32], the rotors are assembled on the underside of the motors mounted on the bottom of the arms, as shown in Fig. 1(a). This configuration is called the inverted rotors and is known to increase the propulsion performance [33], [34]. The rotor (DALPROP 3045) has two untwisted rectangular blades of constant chord $c = 16$ mm with a fixed blade pitch angle of 23°, and the corresponding solidity ($\sigma = N_b c/\pi R_r$; where $N_b$ is the number of rotor blades) of the rotor is 0.268. The brushless DC motors for rotating the rotors were driven by an electronic speed controller (ESC) controlled by a pulse width modulation (PWM) signal to adjust the motor speed. The rotational speed of the rotor, Ω, was measured by a

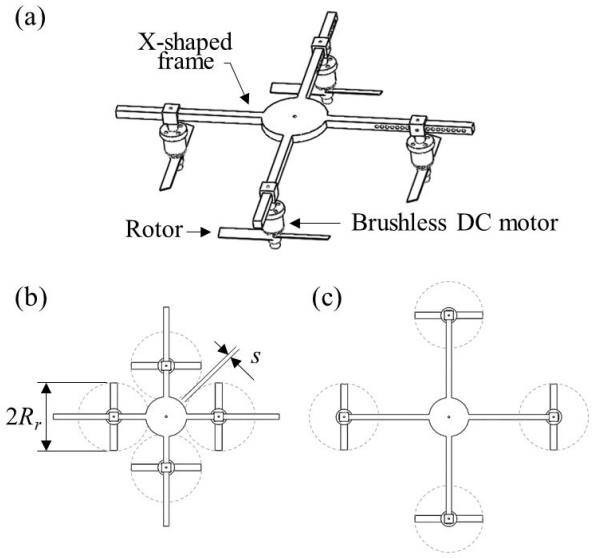


**FIGURE 1.** Details of the quadrotor UAV model: (a) three-dimensional view, (b) top view for $s/R_r = 0.13$, (c) top view for $s/R_r = 2.37$. Here, the dashed circles in Figs. 1(b) and 1(c) indicate the trajectories of the rotor tip movement.

tachometer and varied from 8100 to 12865 rpm. The corresponding rotor tip speed ($V_{\text{tip}} = \Omega R_r$) and Reynolds number ($Re = V_{\text{tip}} c/\nu$; where $\nu$ is the kinematic viscosity of air) were about 32.2 m/s $\leq V_{\text{tip}} \leq$ 51.2 m/s and 34000 $\leq Re \leq$ 54000, respectively. By regulating the duty ratio of the PWM signal with a feedback control loop, the rotational speed of the rotor was maintained within approximately ±50 rpm of the desired value. Note that the rotational speeds of the four rotors were each independently adjusted, and thus the phases of the four rotors were not synchronized with each other.

## III. EXPERIMENTAL SETUP

### A. WAKE VELOCITY MEASUREMENTS

The experimental setup for measuring the velocity fields in the wake of the quadrotor UAV model is shown schematically in Fig. 2(a). The experiment was conducted in a closed chamber of 1.2 m width, 1.2 m length, and 1.2 m height, which was made of transparent acrylic resin to provide the necessary optical access. A cylindrical aluminum rod was mounted in the center of the chamber ceiling and extended 0.6 m into the chamber to support the UAV model. To minimize the interference caused by the support, the rod having a very small diameter of 4 mm (about 5% of rotor diameter) was attached to the center of the X-shaped frame. The distance between the UAV model and the chamber surfaces was kept more than eight times of the rotor diameter, thus confirming the negligible ground, ceiling and wall effects [35]–[40]. The DPIV system used in this study consisted of a Nd:YAG laser (SpitLight PIV Compact 400) operating at 180 mJ, a CCD camera (Vieworks VH-4MC) with a 2048 pixel × 2048 pixel resolution, a timing hub (Integrated Design Tools XS-TH), and a fog generator (SAFEX Fog Generator 2010). The present system was nearly the same as that successfully

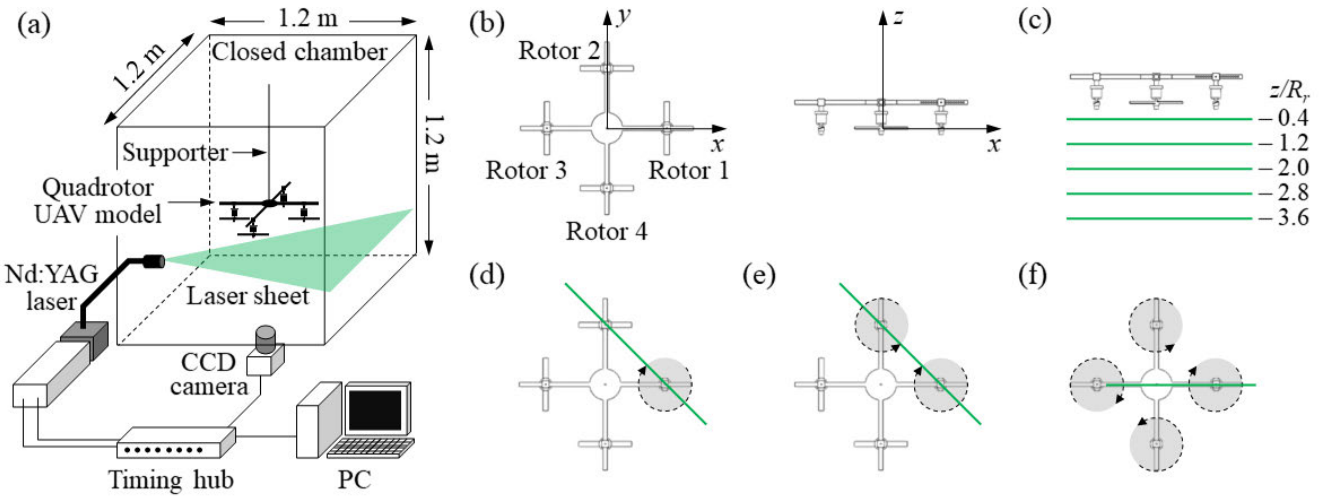


**FIGURE 2.** (a) Schematic diagram (not to scale) of the experimental setup for the wake velocity measurements (for brevity, Fig. 2(a) only illustrates the case of measuring the velocity field in a horizontal plane). (b) The coordinate system and numbering of the rotors used in this study. (c) Location of the horizontal measurement planes. (d-f) Location of the vertical measurement planes for $N_r$ = (d) 1, (e) 2, and (f) 4, where $N_r$ denotes the number of rotating rotor(s). Here, in Figs. 2(d) – 2(f), the gray circle indicates the area swept by the rotor blades rotating in the direction of the dashed arrow.

used in our earlier studies [41]–[46]. The fog generator produced liquid droplets of approximately 1 $\mu$m in diameter, which were introduced in the chamber and used as tracing particles. The laser sheet of 3 mm thickness illuminated the tracing particles within the measurement planes. The reflection of the laser sheet from the UAV model was minimized by painting the model surface matt black, as was applied in our previous works [45], [46]. Figs. 2(b) – 2(f) shows the coordinate system used throughout this paper and the location of the measurement planes. As shown in Fig. 2(b), the origin of the coordinates is located at the center of the UAV model on the rotor-tip path plane (i.e., the $z$ coordinate of the rotor-tip path plane is set to zero as shown on the right of Fig. 2(b)). Note that the rotors are numbered in a counterclockwise direction starting with the rightmost rotor. The wake velocity field was measured in the five horizontal planes at $z/R_r = -0.4, -1.2, -2.0, -2.8$, and $-3.6$ (Fig. 2(c)). The wake velocity measurements were conducted for three cases: when only one rotor rotated while the other three rotors remained stationary (i.e., $N_r = 1$, where $N_r$ is the number of rotating rotor(s)), when two adjacent rotors rotated in opposite directions while the other two rotors remained stationary (i.e., $N_r = 2$), and when all the four rotors rotated (i.e., $N_r = 4$). In all three cases, the rotational speed of the rotor and normalized rotor separation distance were varied from 8100 rpm to 12865 rpm and from 0.13 to 2.37, respectively, as mentioned above. Depending on the case, the velocity field in the wake was measured in different vertical plane as shown in Figs. 2(d) – 2(f). For $N_r = 2$ (Fig. 2(e)) and 4 (Fig. 2(f)), the location of the vertical measurement planes was determined so that the plane aligns with the direction of wake deflection while passing through the center of rotor 1. The size of the field of view (FOV) was varied between 110 mm and 260 mm depending on the measurement plane. An iterative cross-correlation analysis was performed from an initial interrogation window size of 64 pixel × 64 pixel to a final interrogation window size of 32 pixel × 32 pixel with 50% or 75% overlap. The corresponding spatial resolution ranged from 1.16% to 1.32% of the rotor diameter, depending on the measurement plane. Spurious vectors, or outliers, were detected by applying a local median filter, which rejected vectors greater than three times the root mean square (RMS) of a 3 × 3 window. The outliers were replaced with linearly interpolated values from the neighboring vectors. 2000 image pairs were acquired at 7 Hz with a time interval between two successive images of 10 $\mu$s and averaged to obtain a fully converged velocity field. The image acquisition rate was chosen not equal to the harmonics of the rotor blade passing frequencies to ensure that the measured mean velocity fields were not biased to a specific rotor blade phase. Note that the blade passing period of the rotor ranges from 0.0023 to 0.0037 s in the rotational speed range of 8100 to 12865 rpm, and thus the instantaneous velocity fields used in the averaging included from 77140 to 122510 periods of blade passing. The flow-field statistics, such as mean velocity and RMS velocity fluctuations, were extracted at arbitrary locations including the point of maximum RMS velocity fluctuations, and then plotted against the number of image pairs to check the convergence of the results. The oscillations in the flow-field statistics ceased when the number of image pairs reached about 1500, which is well below the number of image pairs used in the time averaging process. The measured time-averaged velocity fields were therefore considered to be converged.

### B. THRUST MEASUREMENTS

Fig. 3 shows a schematic diagram of the experimental setup for measuring the thrust force acting on the quadrotor

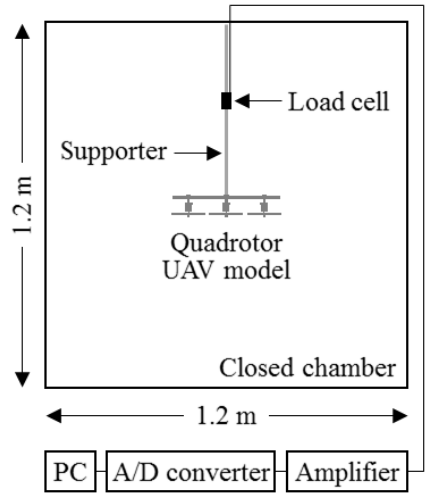


**FIGURE 3.** Schematic diagram (not to scale) of the experimental setup for the thrust measurements.

UAV model. The thrust force was measured in the same chamber as that used for measuring the velocity fields in the wake. Note that both the thrust and wake velocity measurements were performed simultaneously to obtain the correlation between the thrust generated and the measured velocity field. The thrust on the UAV model was measured using a high-accuracy load cell (CAS BCL-1L) attached to the supporter. The measured data were transferred to a computer through an amplifier (VISHAY 2310B) and an A/D converter (NI PICe-6351) and then averaged for 70 s per measurement to obtain a fully converged mean thrust force. The calibration curve was linear in the range of 0 – 10 N, and the measurement was repeated three times. The uncertainty of the measurement was ±2.3%.

## IV. EXPERIMENTAL RESULTS

### A. WAKE VARIATIONS

#### 1) OVERALL WAKE EVOLUTION

To understand the overall three-dimensional structure of the wake flow, multiple two-dimensional velocity fields were measured at various streamwise (negative $z$) positions depicted in Fig. 2(c). Fig. 4 shows the streamwise variations in the normalized mean vorticity contours for $N_r = 1$, 2, and 4 at $Re = 34000$. Here, the normalized rotor separation distance was kept to a minimum of $s/R_r = 0.13$ to maximize the effect of rotor-rotor interaction on the wake structure. For $N_r = 1$ at $z/R_r = -0.4$, the flow velocity induced by the clockwise rotation of the rotor 1 (see Fig. 2(b) for the numbering of the rotors) causes the generation of negative (clockwise) vorticity in the inboard region of the blade. In the tip region of the rotor, however, the flow velocity decreases radially outward from the rotor center (see the inset of Fig. 4(a)) due to the tip effect at the end of the blade so that the positive vorticity is concentrated there. As the rotor wake progresses downstream, i.e., with decreasing $z/R_r$, the tip induced vorticity is rapidly attenuated by turbulent diffusion. The negative vorticity induced by the rotation of the rotor 1 remains concentrated around the rotor center irrespective of $z/R_r$, indicating that the rotor wake convects vertically down and parallel to the z-axis.

For $N_r = 2$ at $z/R_r = -0.4$, the two rotors (1 and 2) rotating in opposite directions induce the generation of negative and positive vortices in the inboard region of the rotor disk 1 and 2, respectively. As the wake develops downstream, the cores of the two inboard vortices move toward each other along the diagonal line connecting the centers of rotors 1 and 2, suggesting that the wakes of rotor 1 and 2 are inclined toward each other. To find out the reason of the wake deflection, for $N_r = 2$ at $z/R_r = -2.0$, the mean velocity vectors are shown in Fig. 5(a) along with the normalized mean vorticity contour. The figure shows that as the flows emerging from the two counter-rotating rotors merge, a high-speed outward sidewash is formed between rotors 1 and 2 along the positive diagonal direction (i.e., toward the first quadrant of the $xy$-plane). Then the high-speed sidewash would induce a low-pressure region between the inboard vortices (green region in Fig. 5(a)), resulting in the rotor wakes to be tilted toward each other. It is interesting to note that, unlike when $N_r = 1$, the inboard vortices are distorted along the edge of the sidewash where the shear rate is high.

For $N_r = 4$, adjacent rotors (e.g., rotors 1 and 2) rotate in opposite directions and diagonally opposite rotors (e.g., rotors 1 and 3) rotate in the same direction. Thus, two negative and two positive inboard vortices are alternately formed at $z/R_r = -0.4$, as shown in the first row of Fig. 4(c). With decreasing $z/R_r$, the cores of the four inboard vortices move from the center of each rotor to the center of the UAV model. This indicates that the wakes from individual rotors deflect toward the center of the UAV model as they develop downstream, which can be explained in Fig. 5(b) as follows: The interaction between the rotor wakes produces outward sidewash (between rotors 1 and 2 and between rotors 3 and 4) and inward sidewash (between rotors 1 and 4 and between rotors 2 and 3) flows, which would lead to the formation of low-pressure regions between each of the four rotors (green regions in Fig. 5(b)). The pressure imbalance for each inboard vortex then causes the rotor wakes to be pulled toward the center of the UAV model. For example, the wake interaction between rotors 1 and 2 and between rotors 2 and 3 generates a high-speed outward sidewash along the positive diagonal (see the right inset of Fig. 5(b)) and a high-speed inward sidewash along the negative diagonal (see the left inset of Fig. 5(b)). Then the wake of rotor 2 would be pulled downward (i.e., toward the center of the UAV model) by the low-pressure regions formed on the lower right and lower left of the inboard vortex from the rotor 2 (see green regions in the insets of Fig. 5(b)). Similar to when $N_r = 2$, the distortion of the inboard vortices is observed along the edge of the outward sidewash, as shown in Fig. 5(b).

#### 2) WAKE FLOW FIELDS FOR $N_r = 1$

Fig. 6(a) shows the variation of the normalized mean axial (i.e., normal to the rotor disk) velocity profiles for $N_r = 1$ and

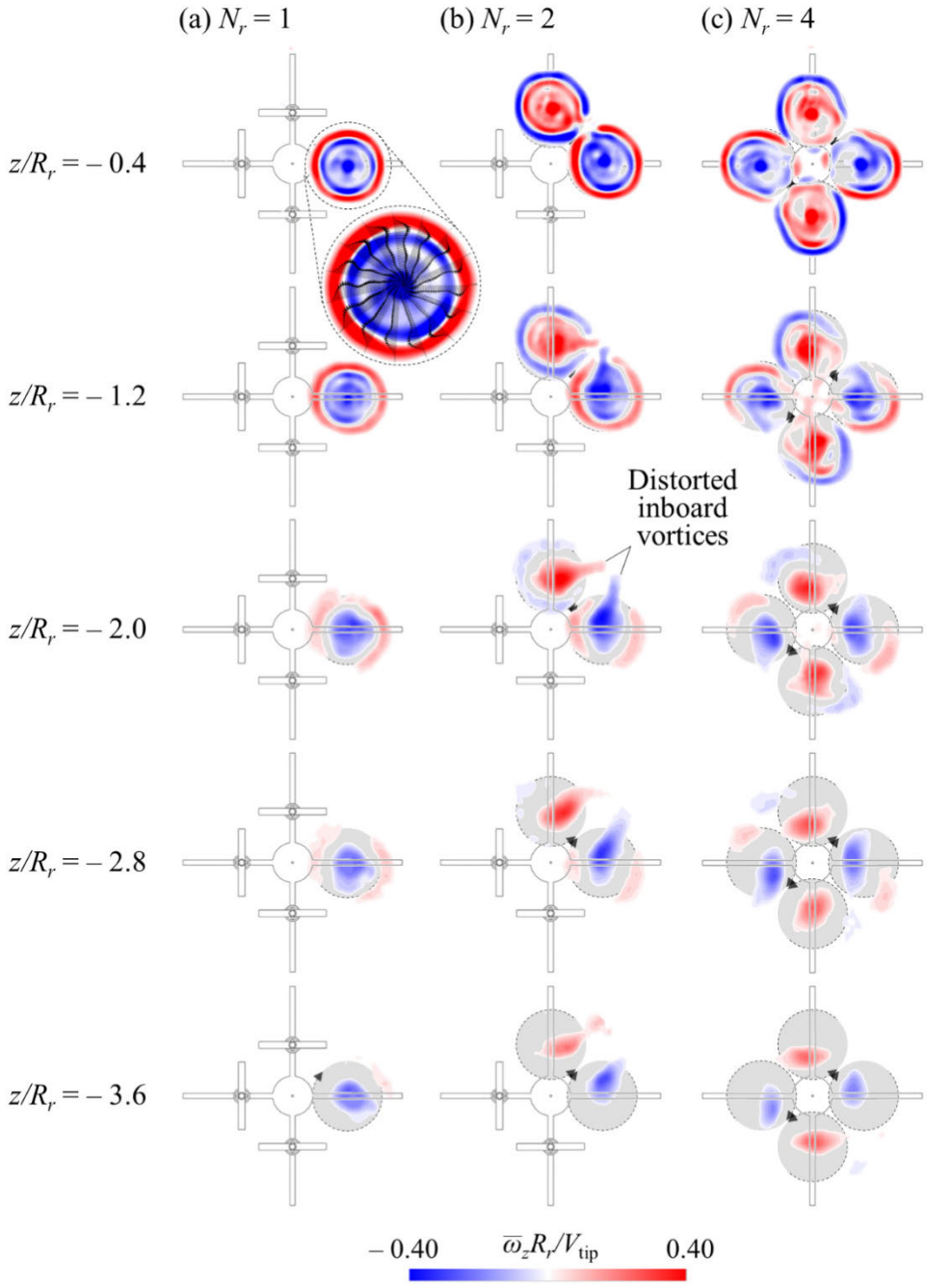


**FIGURE 4.** Contours of normalized mean vorticity $\bar{\omega}_z R_r/V_{tip}$ for $N_r$ = (a) 1 (first column), (b) 2 (second column), and (c) 4 (third column) at varying $z/R_r$, where $\bar{\omega}_z$ is the mean vorticity in $z$-direction. Here, the normalized rotor separation distance was fixed as $s/R_r = 0.13$ for all cases. Note that each row denotes different values of $z/R_r$. The gray circle indicates the area swept by the rotor blades rotating in the direction of the dashed arrow. The inset of Fig. 4(a) shows the enlarged view along with the mean velocity vectors.

$Re = 34000$ at $s/R_r = 0.13$, 1.18, and 2.37. For comparison, let us now introduce a local $m$-coordinate aligned with the measurement plane beginning at the center of the rotor 1, as shown in the inset of Fig. 6(b). The velocity profiles at different $s/R_r$ collapse well for each value of $z/R_r$ when plotted against $m/R_r$, indicating that for $N_r = 1$ the wake flow field is independent of the normalized rotor separation distance. This is because the nonrotating rotors 2, 3, and 4 induce no flow at zero freestream velocity and thus the wake flow of the rotor 1 could hardly interact with those of other rotors. The rotor blade used in this study is rectangular and untwisted, as described in Section II, and thus the axial

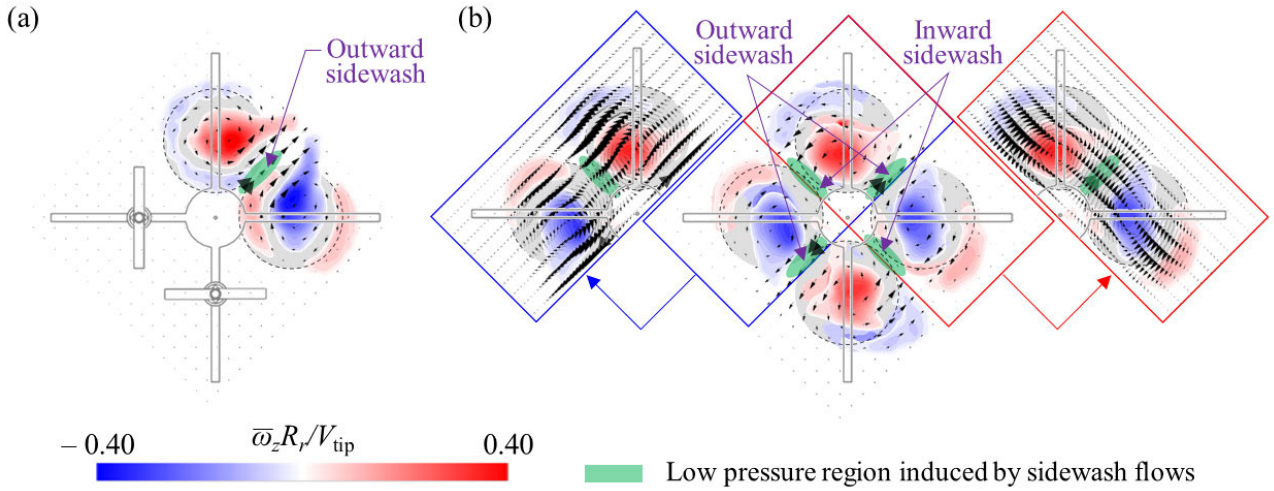


**FIGURE 5.** Mean velocity vectors and contours of the normalized mean vorticity $\bar{\omega}_z R_r/V_{tip}$ at $z/R_r = -2.0$ for $N_r$ = (a) 2 and (b) 4. Here, the normalized rotor separation distance was fixed as $s/R_r = 0.13$ for all cases. The gray circle indicates the area swept by the rotor blades rotating in the direction of the dashed arrow. In Fig. 5(b), the insets in the red and blue boxes are given for better visualization of the outward sidewash and the inward sidewash between the rotor wakes, respectively.

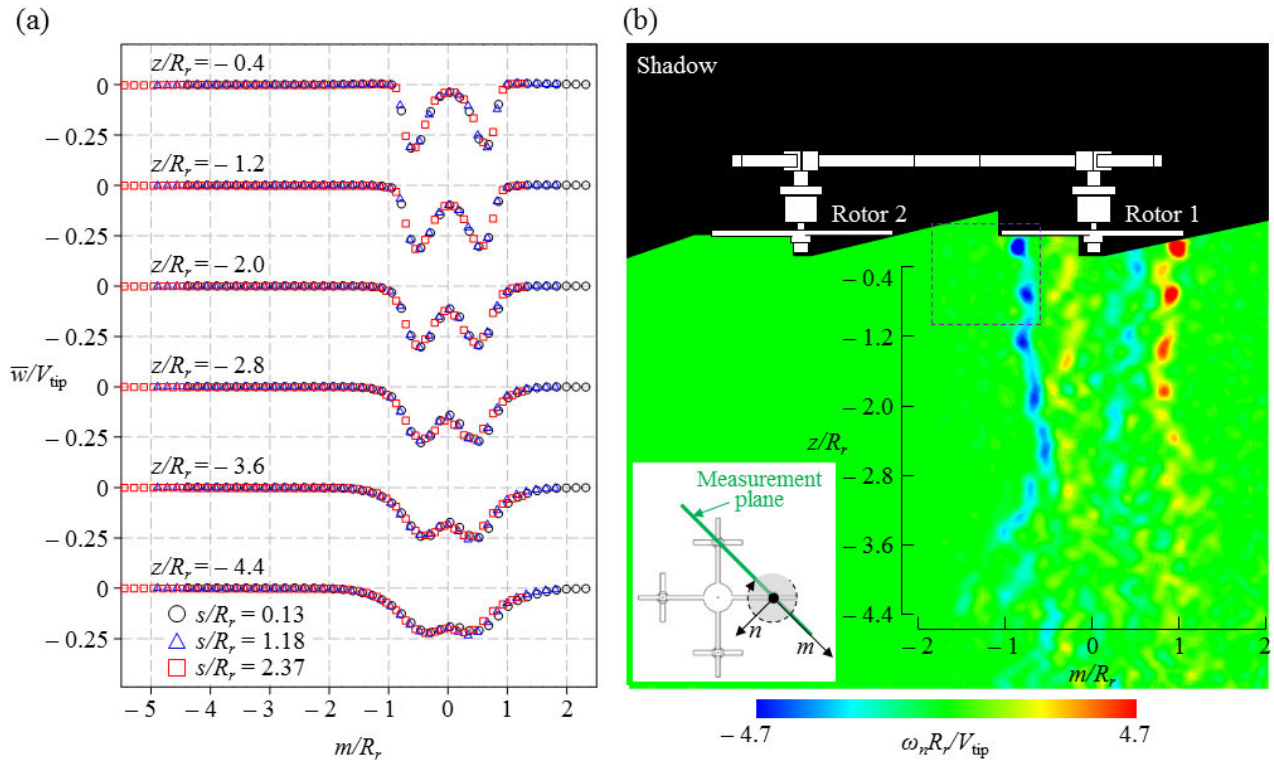


**FIGURE 6.** (a) Profiles of the normalized mean axial velocity $\bar{w}/V_{tip}$ for $N_r = 1$ and $Re = 34000$ at $s/R_r = 0.13$ (black circles), 1.18 (blue triangles), and 2.37 (red squares). (b) Contours of normalized instantaneous vorticity $\omega_n R_r/V_{tip}$ at $s/R_r = 1.18$. The lower left inset of Fig. 6(b) shows the location of the measurement plane and the coordinate axes used in Figs. 6 and 7. The gray circle in the inset indicates the area swept by the rotor blades rotating in the direction of the dashed arrow.

velocity distribution between the blade root (i.e., $m/R_r = 0$) and the blade tip (i.e., $|m/R_r| = 1$) is approximately triangular in the close vicinity of the rotor-tip path plane at $z/R_r = -0.4$. The peak axial velocity at a given $z/R_r$ gradually decreases downstream thereby forming a jet-like flow. With decreasing $z/R_r$, two jet-like flows, which are symmetric about the rotational axis of the rotor 1 ($m/R_r = 0$), spread (i.e., the width of each jet-like flow increases) and merge together. The decay and spread of jet-like flow was also observed in the rotor wake flow at low

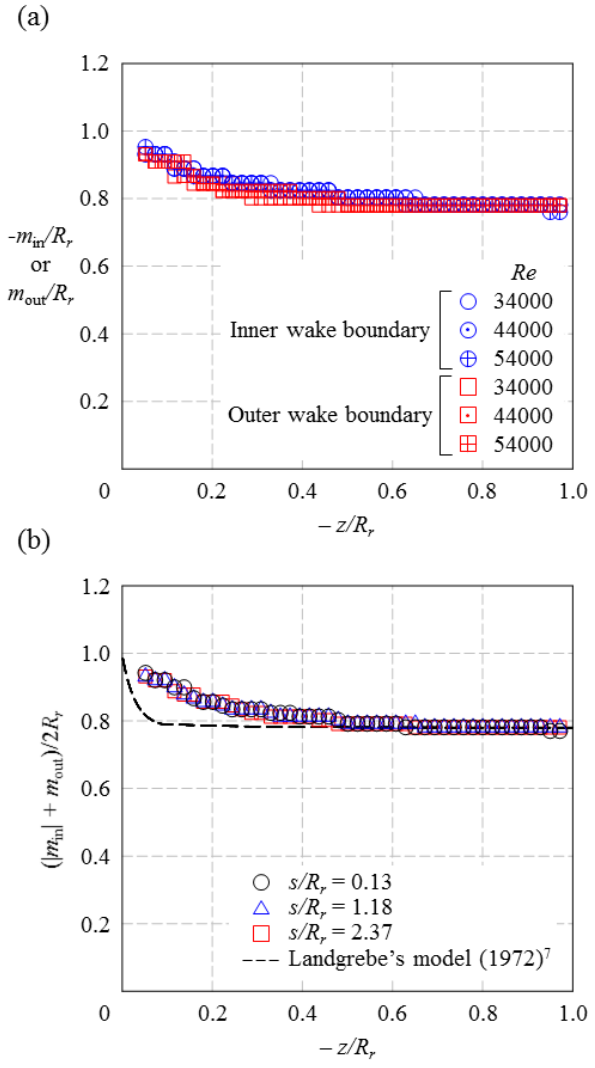


**FIGURE 7.** (a) Inner and outer wake boundaries below the rotor 1 at $s/R_r = 2.37$ for $Re = 34000$, 44000, and 54000. $m_{in}$ and $m_{out}$ denote the $m$-coordinates of the inner and outer wake boundaries, respectively. (b) Mean wake boundaries for $Re = 34000$ at $s/R_r = 0.13$ (black circles), 1.18 (blue triangles), and 2.37 (red squares). The black dashed curve denotes the wake boundary obtained from the Landgrebe's model [7] under the conditions of the present study ($C_{T,1} = 0.033$, $\sigma = 0.268$, $N_b = 2$, $\theta_{tw} = 0$), where the number in the subscript denotes the number of rotating rotor(s) and $\theta_{tw}$ is the blade twist.

Reynolds number [47]. The rotor wake convects vertically down without any lateral motion, which is consistent with our observations in Fig. 4(a). Fig. 6(b) shows the instantaneous normalized vorticity contours at $s/R_r = 1.18$. The tip vortices generated at both blade tips of the rotor 1 convect downstream, thereby forming helical structures. Within the tip-vortex helices, the wake vortices are observed in the streamwise direction in the rotor reference frame, whose vorticity is opposite-signed to those of the adjacent tip vortices. The formation and evolution of wake vortices similar to those shown in this study has also been observed in the flow around a low-aspect-ratio wing at high angles of attack and low Reynolds numbers [48], [49]. The symbols in Fig. 7(a) show the inner and outer wake boundaries below the rotor 1 at $s/R_r = 2.37$ for $Re = 34000$, 44000, and 54000. In this study, the inner and outer wake boundaries are defined as the time-averaged trajectories of the tip vortices on the side of the adjacent rotor and on the opposite side, respectively. That is, for the rotor 1, the inner and outer wake boundaries denote the time-averaged trajectories of the tip vortices containing negative and positive normalized vorticities $\omega_n R_r / V_{tip}$, respectively (see Fig. 6(b)). The time-averaged trajectory was identified by tracing the peak time-averaged vorticity. Fig. 7(a) shows the inner and outer wake boundaries of the rotor 1 in the $mz$-plane. The inner and outer wake boundaries for the same $Re$ almost coincide with each other, as can be expected from the axisymmetry of the velocity fields described above. The wake boundaries from different Reynolds numbers nearly coincide, indicating that the wake boundary is little affected by the Reynolds number (i.e., the rotational speed of the rotor) in the $Re$ range investigated. Thus, only data from $Re = 34000$ will be considered in detail in this paper. The wake radius defined by the distance from the rotational axis (i.e., $m/R_r = 0$) to the wake boundary at a given $z/R_r$ asymptotically decreases as the wake convects downstream, giving the wake contraction ratio (i.e., the ratio of the diameter of the wake at the vena contracta to the diameter of the rotor) of 0.78. This value agrees very well with previous experimental data [7], [11], [50], [51]. To determine the effect of the normalized rotor separation distance on the wake boundary, the mean wake boundaries are shown in Fig. 7(b) at $s/R_r = 0.13$, 1.18, and 2.37. The mean wake boundary was obtained by averaging the inner and outer wake boundaries at each $s/R_r$. The mean wake boundaries at different $s/R_r$ collapse well, indicating that for $N_r = 1$ the wake geometry is independent of the normalized rotor separation distance. The black dashed curve in Fig. 7(b) is the wake boundary predicted by the Landgrebe's model [7] under the conditions of the present study ($C_{T,1} = 0.033$, $\sigma = 0.268$, $N_b = 2$, $\theta_{tw} = 0$), where the number in the subscript denotes the number of rotating rotor(s) and $\theta_{tw}$ is the blade twist. The wake contraction ratio calculated from the model is 0.78, which agrees very well with the measured ones. The detailed wake geometry predicted by the model, however, differs from the measured ones, especially in the near-wake region of $z/R_r > -0.4$; that is, the radius of the wake predicted by the model contracts much faster than the measured ones in the near-wake region, indicating that the Landgrebe's model [7] is inaccurate in describing a rotor wake geometry of a quadrotor UAV. Moreover, when multiple rotors rotate, the rotor wake interaction makes the wake geometry non-axisymmetric and more complicated [1]–[6], [52], which further limits the applicability of the model to a quadrotor UAV. The inapplicability of the Landgrebe's model [7] to the present UAV may be due to the fact that the model was developed for a helicopter rotor. For a helicopter rotor, a tip Mach number generally exceeds 0.3, and thus the flow near the blade tip is compressible [8], [53]. However, the rotors

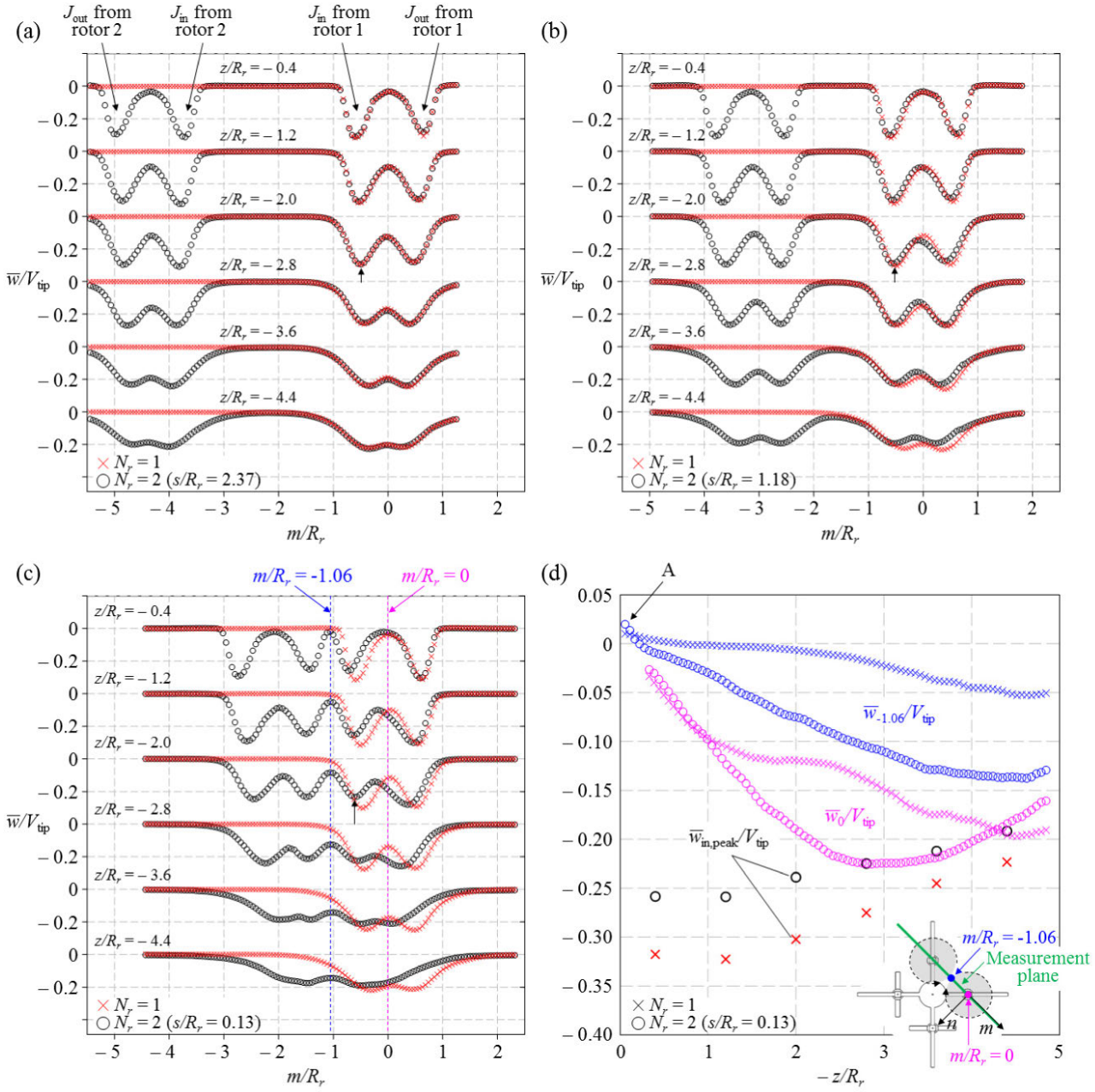


**FIGURE 8.** Profiles of the normalized mean axial velocity $\bar{w}/V_{tip}$ for $N_r = 2$ and $Re = 34000$ at (a) $s/R_r = 2.37$, (b) 1.18, and (c) 0.13. Profiles for $N_r = 1$ at corresponding $s/R_r$s are also shown for comparison as red crosses. Here $J_{in}$ and $J_{out}$ denote the inner and outer jet-like flows, respectively. Black arrows pointing up denote the positions of the peak axial velocity in $J_{in}$ and $J_{out}$, respectively, from the rotor 1 at the same $z/R_r = -2.0$. (d) Variations of $\bar{w}_{-1.06}/V_{tip}$ (blue symbols), $\bar{w}_0/V_{tip}$ (pink symbols), and the peak $\bar{w}/V_{tip}$ in $J_{in}$ from rotor 1 ($\bar{w}_{in,peak}/V_{tip}$) with $z/R_r$. Here, $\bar{w}_{-1.06}$ and $\bar{w}_0$ is the mean axial velocity along $m/R_r = -1.06$ (the centerline between the centers of rotor 1 and 2) and $m/R_r = 0$ (the rotational axis of rotor 1) at $s/R_r = 0.13$, respectively. Note that there is no velocity data along $m/R_r = 0$ in the range of $-0.27 < z/R_r < 0$ where the rotor hub is located. The lower right inset shows the location of $m/R_r = -1.06$ and 0 at $s/R_r = 0.13$.

typically used on small-scale UAVs, such as those manufactured by DJI, APC, and GoPro, operate at tip Mach numbers below 0.23 [54], indicating that the flow around UAV rotor blades is incompressible. Since compressibility is known to play a crucial role in altering the details of vortex formation [55], [56], the flow around UAV rotor blades should differ from that around helicopter rotor blades. Thus, in Section IV-B, a new model will be proposed to accurately predict the rotor wake geometry of the quadrotor UAV model in the absence of compressibility effects.

### 3) WAKE FLOW FIELDS FOR $N_r = 2$

Fig. 8 shows the variation of the normalized mean axial velocity profiles for $N_r = 2$ with varying $s/R_r$. In order to compare

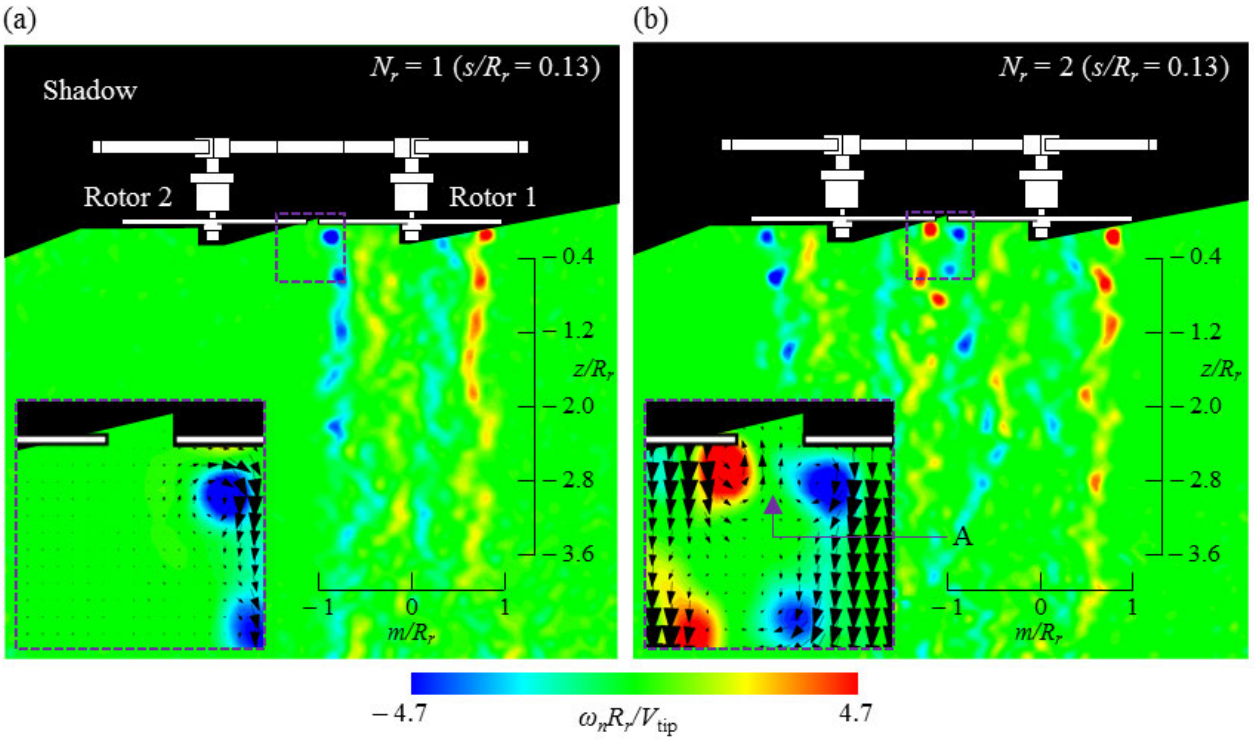


**FIGURE 9.** Contours of normalized instantaneous vorticity $\omega_n R_r/V_{tip}$ for (a) $N_r = 1$ and (b) 2 at $s/R_r = 0.13$. The lower left inset shows the velocity vectors in the region enclosed by the dotted rectangle.

the profiles for $N_r = 2$ with those for $N_r = 1$, the profiles at corresponding $s/R_r$s for $N_r = 1$ are plotted as red crosses in Fig. 8. Note that the local $m$-coordinate for $N_r = 2$ is the same as that for $N_r = 1$ (see the inset of Fig. 6(b)): For example, at $s/R_r = 2.37$, rotor tips are located at $(m/R_r, z/R_r) = (\pm 1, 0)$ for the rotor 1 and at $(m/R_r, z/R_r) = (-3.37, 0)$ and (-5.37, 0) for the rotor 2. At the largest normalized rotor separation distance of $s/R_r = 2.37$, two pairs of jet-like flows are formed from the rotors 1 and 2 in the near wake as shown in Fig. 8(a). Each pair of jet-like flows consist of an inner one ($J_{in}$) on the side of the adjacent rotor and an outer one ($J_{out}$) on the opposite side. The inner and outer jet-like flows decay and spread as they move downstream and then merge each other, as was observed for $N_r = 1$. The axial velocity profiles in the wake of rotor 1 show almost no difference between $N_r = 1$ and 2, indicating that, for $N_r = 2$, there is little interaction between the rotor wakes at this value of $s/R_r$. However, as $s/R_r$ decreases from 2.37 (Fig. 8(a)) to 0.13 (Fig. 8(c)), the position of peak axial velocity in $J_{in}$ and $J_{out}$ from rotor 1 moves toward the adjacent rotor (i.e., in the negative $m$-direction) at a given $z/R_r$. For example, at $z/R_r = -2.0$, the $m/R_r$ coordinates of the position of peak axial velocity in $J_{in}$ from the rotor 1 are $-0.494$, $-0.535$ and $-0.622$ for $s/R_r = 2.37$, 1.18, and 0.13, respectively (see the black arrows pointing up in Figs. 8(a) to 8(c)). Due to the deflection of $J_{in}$ and $J_{out}$ described above, the axial velocity profiles of the wake of rotor 1 become gradually asymmetric with respect to the rotational axis of rotor 1 ($m/R_r = 0$) as $s/R_r$ decreases. However, the symmetry of the axial velocity profile about the centerline ($m/R_r = -2.18$, $-1.59$, and $-1.06$ for $s/R_r = 2.37$, 1.18, and 0.13, respectively) between rotors 1 and 2 is maintained independent of the normalized rotor separation distance.

When the rotor-rotor interaction is maximized at $s/R_r = 0.13$, the inner jet-like flows of rotors 1 and 2 merge at the centerline ($m/R_r = -1.06$; the blue dashed line in Fig. 8(c)), thus increasing the axial velocity as the wake convects downstream (see the blue circles in Fig. 8(d)). Even when there is no rotor-rotor interaction ($N_r = 1$), the axial velocity increases along $m/R_r = -1.06$ (see the blue X symbols in Fig. 8(d)), which is due to the spread of the jet-like flow shown in Fig. 8(c). Note that, as can be found by comparing the blue symbols in Fig. 8(d), the axial flow between rotors 1 and 2 is more accelerated in the streamwise direction by the merging of the inner jet-like flows in the presence of rotor-rotor interaction than by the spread of the jet-like flow in the absence of rotor-rotor interaction. For $N_r = 1$, the merging of $J_{in}$ and $J_{out}$ from rotor 1 occurs at the rotational axis of rotor 1 ($m/R_r = 0$; see the pink dashed line in Fig. 8(c)), and accordingly, the axial velocity increases along $m/R_r = 0$ as the wake of rotor 1 develops downstream (see the pink X symbols in Fig. 8(d)). For $N_r = 2$, on the other hand, the axial velocity increases along $m/R_r = 0$ (see the pink circles in Fig. 8(d)) as the position of peak

axial velocity in $J_{out}$ from rotor 1 moves in the negative $m$-direction. Comparing the pink symbols in Fig. 8(d), it can be seen that the axial velocity along the rotor axis is larger over a wide range of $z/R_r$ when the outer jet-like flow is deflected by the rotor-rotor interaction than when the jet-like flows merge with no rotor-rotor interaction. The above results indicate that a strong interaction between the rotor wakes induces a high-speed streamwise flow on either side of $J_{in}$ from rotor 1. To examine the effect of the high-speed flow around $J_{in}$ induced by the interaction on the evolution of the inner jet-like flow, the normalized peak axial velocity in $J_{in}$ from rotor 1 ($\bar{w}_{in,peak}/V_{tip}$) at $s/R_r = 0.13$ for $N_r = 2$ is compared with that for $N_r = 1$ in Fig. 8(d). It can be seen that the magnitude of $\bar{w}_{in,peak}/V_{tip}$ for $N_r = 2$ remains smaller than that for $N_r = 1$. As the wake convects downstream (i.e., with decreasing $z/R_r$), the difference in the magnitude of $\bar{w}_{in,peak}/V_{tip}$ between $N_r = 1$ and 2 gradually decreases from 18.6% (at $z/R_r = -0.4$) to 14.1% (at $z/R_r = -4.4$), which indicates that the inner jet-like flow decays more slowly for $N_r = 2$ than for $N_r = 1$. The slow decay of $J_{in}$ in the presence of strong rotor-rotor interaction could be due to the addition of streamwise momentum supplied by the high-speed flow around the inner jet-like flow described above. Note that the magnitude of $\bar{w}_{in,peak}/V_{tip}$ remains almost constant or rather, increases slightly in the very near wake ($-1.2 \le z/R_r \le -0.4$), which may be due to the wake contraction (i.e., the decrease in the wake diameter) in the streamwise direction (see Fig. 7).

It needs to be emphasized that the flow between the rotors near the rotor-tip path plane (A in Fig. 8(d)) is in the positive $z$-direction (i.e., opposite to the streamwise direction), and its magnitude is greater for $N_r = 2$ than for $N_r = 1$. To understand how the rotor-rotor interaction induces a stronger flow in the counter-streamwise direction, the contours of normalized instantaneous vorticity for $N_r = 1$ and 2 are shown in Fig. 9. By comparing Figs. 9(a) and 9(b), it can be seen that for $N_r = 2$, a strong upwash (A in Fig. 9(b)) is generated as a result of the local pairing of tip vortices of opposite sign. The enhanced upwash flow between rotors 1 and 2 would induce the loss of streamwise momentum in the very near wake, resulting in a weakening of the inner jet-like flow (compare the magnitude of $\bar{w}_{in,peak}/V_{tip}$ at $z/R_r = -0.4$ between $N_r = 1$ and 2 in Fig. 8(d)).

To quantitatively analyze the wake deflection, the inner and outer wake boundaries below the rotor 1 are plotted in Figs. 10(a) and 10(b), respectively, with varying $s/R_r$. For comparison, the wake boundaries at different $s/R_r$s for $N_r = 1$ are averaged and plotted as red crosses in Fig. 10. As mentioned earlier, at $s/R_r = 2.37$, there is little interaction between the rotor wakes, and thus the wake boundaries for $N_r = 1$ and 2 almost overlap with each other. Note that one end of the wake boundary is shown to be fixed at the rotor tip because the tip vortex originates from the tip of the blade. That is, on the rotor-tip path plane of $z/R_r = 0$, the normalized $m$-coordinates of the inner and outer wake boundaries approach $m_{in}/R_r = -1$ (Fig. 10(a)) and $m_{out}/R_r = 1$

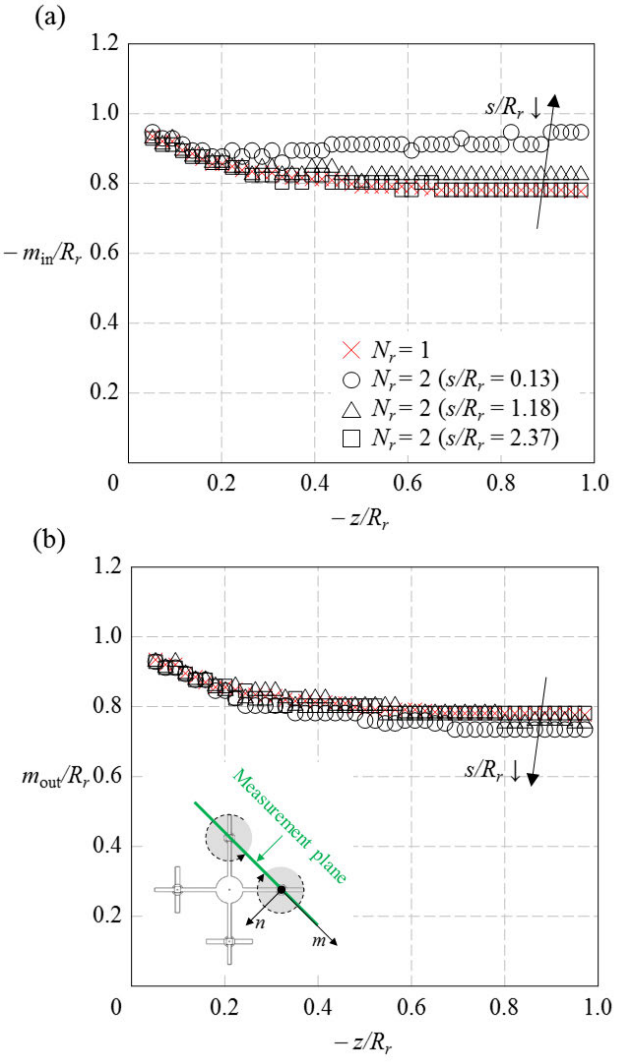


**FIGURE 10.** Variations in the (a) inner and (b) outer wake boundaries below the rotor 1 with the normalized rotor separation distance for $N_r = 2$. Wake boundary for $N_r = 1$ is also shown for comparison as red crosses. The gray circle in the inset of Fig. 10(b) indicates the area swept by the rotor blades rotating in the direction of the dashed arrow.

(Fig. 10(b)), respectively. As the normalized rotor separation distance decreases, the wake of the rotor 1 deflects toward that of rotor 2, resulting in the movement of the inner and outer wake boundaries in the negative $m$-direction (see the inset of Fig. 10(b) for the direction of $m$-coordinate). The magnitude of wake deflection of the inner wake boundary is larger than that of the outer one at small $s/R_r$, which implies that the inner wake boundary is more sensitive to the rotor wake interaction than the outer wake boundary.

#### 4) WAKE FLOW FIELDS FOR $N_r = 4$

When all the four rotors rotate, as described in Section IV-A.1, the wakes from individual rotors deflect toward the center of the UAV model as they develop downstream. Thus, for $N_r = 4$, the location of the measurement plane was determined as shown at the top of Fig. 11(a) so that

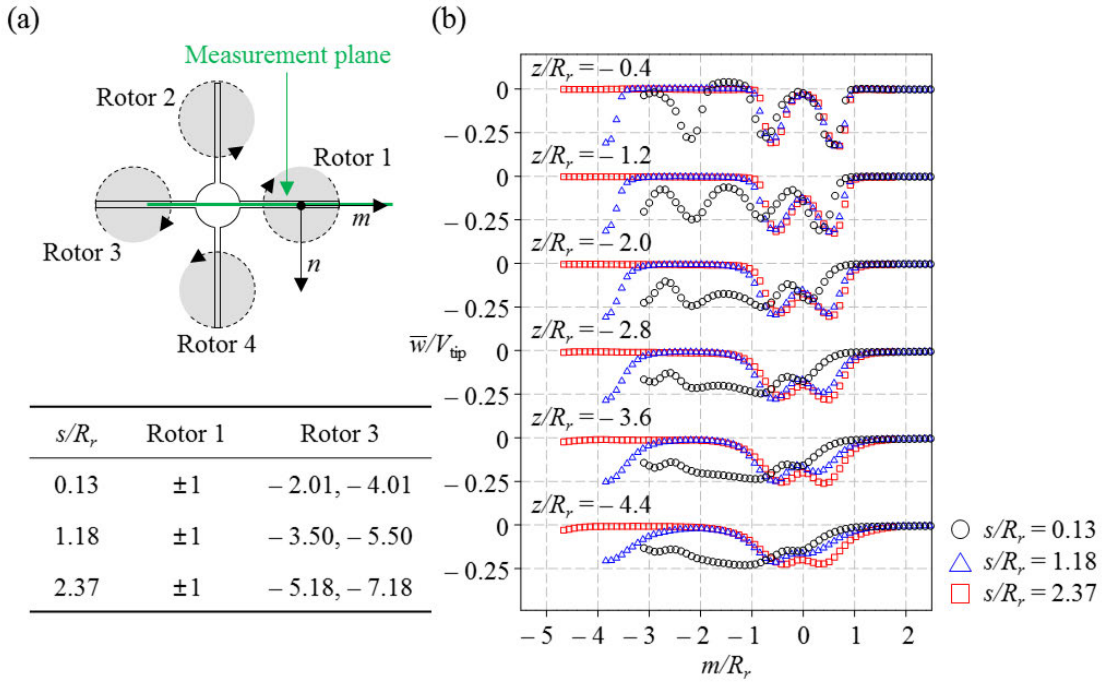


| $s/R_r$ | Rotor 1 | Rotor 3 |
|---|---|---|
| 0.13 | ±1 | – 2.01, – 4.01 |
| 1.18 | ±1 | – 3.50, – 5.50 |
| 2.37 | ±1 | – 5.18, – 7.18 |

**FIGURE 11.** (a) (top) Location of the measurement plane and the coordinate axes used in Figs. 11 to 13 and Fig. 18. The gray circle indicates the area swept by the rotor blades rotating in the direction of the dashed arrow. (bottom) *m*-coordinates of the tips of rotors 1 and 3 on the rotor-tip path plane ($z/R_r = 0$). (b) Profiles of the normalized mean axial velocity $\bar{w}/V_{tip}$ for $N_r = 4$ at $s/R_r = 0.13$ (black circles), 1.18 (blue triangles), and 2.37 (red squares).

the plane aligns with the direction of wake deflection while passing through the center of rotor 1. Accordingly, the local $m$-coordinate is defined differently for $N_r = 4$ from other cases (compare Figs. 6(b), 10(b), and 11(a)). As shown in the table at the bottom of Fig. 11(a), the tips of rotor 1 are located at $(m/R_r, z/R_r) = (\pm 1, 0)$ irrespective of $s/R_r$, whereas the $m$-coordinates of the tips of rotor 3 vary depending on $s/R_r$. Fig. 11(b) shows the normalized mean axial velocity profiles at different $s/R_r$s for $N_r = 4$. Note that here, some part of the wake flow field of the rotor 3 is omitted due to the limited size of the field of view. As shown in Fig. 11(b), the effects of the normalized rotor separation distance on the wake of rotor 1 are similar to those for $N_r = 2$: As $s/R_r$ decreases, the position of peak axial velocity in the inner and outer jet-like flow moves toward the neighboring rotor in the near wake. Similar to when $N_r = 2$, when the four rotors are closest together at $s/R_r = 0.13$, a strong upwash flow from downstream to upstream is locally observed between the rotor tips ($-2.01 < m/R_r < -1$) in the close vicinity of the rotor-tip path plane at $z/R_r = -0.4$.

Fig. 12(a) shows the instantaneous normalized vorticity contour at $s/R_r = 0.13$. It can be seen that an upwash flow is located between the counter-rotating vortices (see A in Fig. 12(a)), as was observed for $N_r = 2$ (see A in Fig. 9(b)). One interesting point is that, for $N_r = 4$, high upwash is formed even where there appear to be no counter-rotating vortex pairs (see B in Fig. 12(a)). This is an important observation for it suggests that the interaction between the inner tip vortices also takes place vigorously in the planes (e.g., $yz$-plane in Fig. 2(b)) other than the plane on which the DPIV measurement was conducted. That is, a strong upwash flow would be obtained by the pairing of tip vortices generated by all the four rotors, thereby forming an upflow region below the center of the UAV model as shown in the lower right inset of Fig. 12(a). The formation of upwash flow in the opposite direction to the induced velocity was also observed at a low $s/R_r$ in the previous studies on multirotor UAVs [2]–[6], [31].

The rotor-rotor interaction, especially the interaction of the vortices emanating from the tip of the rotor blades, affects not only the mean velocity field but also the velocity fluctuation field as follows. Figs. 12(b) and 12(c) show the contours of normalized turbulent kinetic energy (TKE) around the blade tip of rotor 1 for $N_r = 4$ and 1, respectively. From the comparison of the figures, it can be seen that the interaction among the tip vortices of the rotors 1 to 4 increases the turbulence level. This result agrees with those found by Zhou *et al.* [1], who observed that the TKE was enhanced by the interaction of tip vortices for twin rotors. It is worth noting that the inner tip vortices break into smaller vortices for $N_r = 4$ than for $N_r = 1$ (compare the regions represented by a dotted rectangle in Figs. 6(b) and 12(a)). Considering that wing-tip vortex breakdown is promoted by high levels of turbulence [57], in this study, the turbulence generated by rotor-rotor interaction would enhance the breakdown of tip vortices between the rotors.

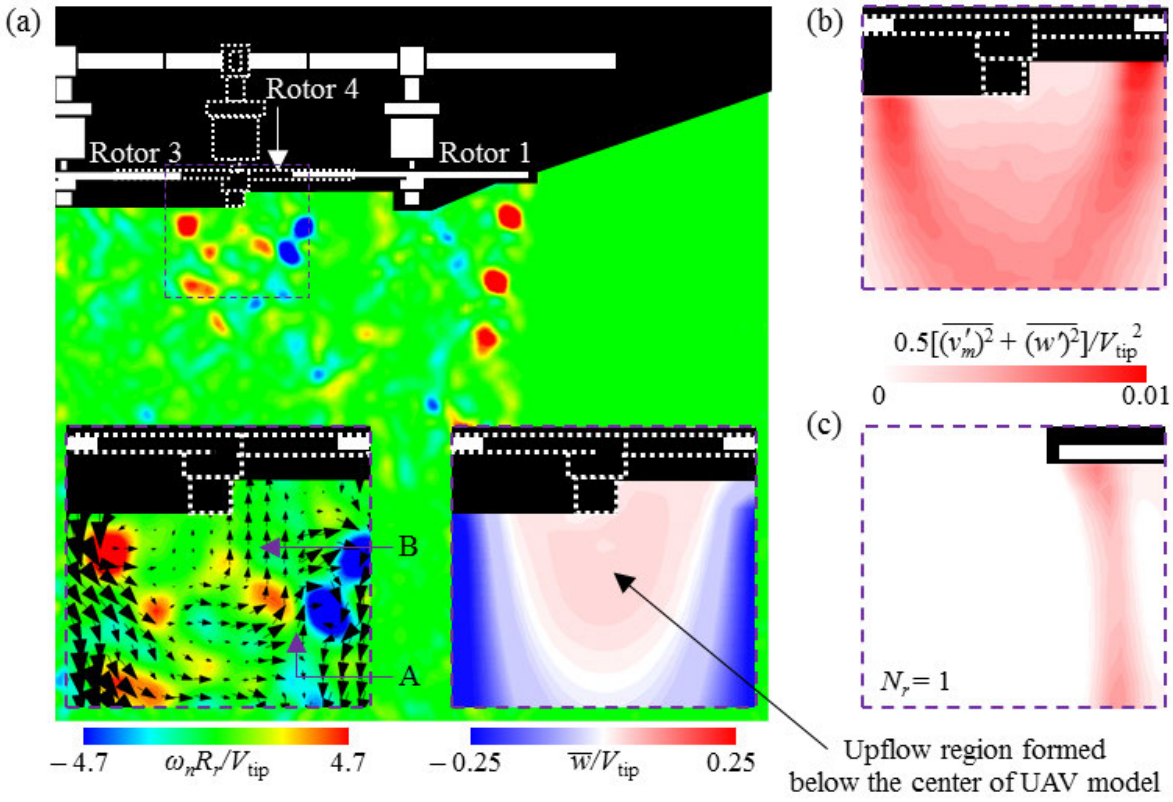


**FIGURE 12.** (a) Contours of normalized instantaneous vorticity $\omega_n R_r/V_{tip}$ for $N_r = 4$ and $Re = 34000$ at $s/R_r = 0.13$. The lower left and lower right insets show the velocity vectors and contours of normalized mean axial velocity $\bar{w}/V_{tip}$, respectively, in the region enclosed by the dotted rectangle. (b,c) Contours of normalized turbulent kinetic energy (TKE) in the region enclosed by the dotted rectangle of (b) Fig. 12(a) and (c) Fig. 6(b). $v_m'$ and $w'$ denote the velocity fluctuations in the $m$ and $z$ directions, respectively. Note that the rotor 4 is placed in front of the measurement plane in the direction of $n$-axis (i.e., perpendicular to the page; see Fig. 11(a)), and is thus shown as dashed lines.

Fig. 13 shows the variations in the inner and outer wake boundaries below the rotor 1 with the normalized rotor separation distance. As was observed in Section IV-A.3, with decreasing $s/R_r$, the wake boundaries deviate more from that with no rotor wake interaction (i.e., $N_r = 1$) toward the neighboring rotor (i.e., in the negative $m$-direction). Note that there is little Reynolds number effect on the wake boundary even when the rotor-rotor interaction is strongest at $s/R_r = 0.13$, as shown in Fig. 13(a). The effect of the number of rotating rotors on the wake geometry can be seen by comparing Figs. 10 and 13 at the same normalized rotor separation distance of $s/R_r = 0.13$. Both the inner (compare open circles in Fig. 10(a) with dotted circles in Fig. 13(a)) and outer (compare open circles in Fig. 10(b) with dotted circles in Fig. 13(b)) wake boundaries deviate more from those for $N_r = 1$ (red crosses in Figs. 10 and 13) as $N_r$ increases. The amount of deviation is greater for the inner wake boundary than the outer wake boundary at the same $N_r$ (compare open circles in Figs. 10(a) and 10(b) for $N_r = 2$, and compare dotted circles in Figs. 13(a) and 13(b) for $N_r = 4$). This is because, as was pointed out in Section IV-A.1, the low pressure formed between the rotor wakes is the cause of the wake boundary deflection: For $N_r = 2$, the low-pressure region is formed on the upper left side of the rotor 1 by the high-velocity sidewash between the wakes of rotors 1 and 2 (see the green region in Fig. 5(a)), whereas for $N_r = 4$, the low-pressure regions are formed on the upper left (between the rotors 1 and 2) and lower left (between the rotors 1 and 4) sides of the rotor 1 (see the green regions in Fig. 5(b)). Thus, the wake of rotor 1 is more strongly attracted for $N_r = 4$ than for $N_r = 2$, resulting in more deflection of the rotor wake. The low-pressure region between the rotor wakes is located closer to the inner jet-like flow than the outer jet-like flow, and consequently the inner wake boundary deviates more from that for $N_r = 1$ than the outer wake boundary.

### B. WAKE MODELING

As pointed out earlier in this paper, the Landgrebe's model [7] has the limitation of the inability to describe the rotor wake geometry of a quadrotor UAV, which is mainly because the model does not reflect the wake interaction between rotors. Considering that the normalized rotor separation distance determines the extent of rotor wake interaction at a given

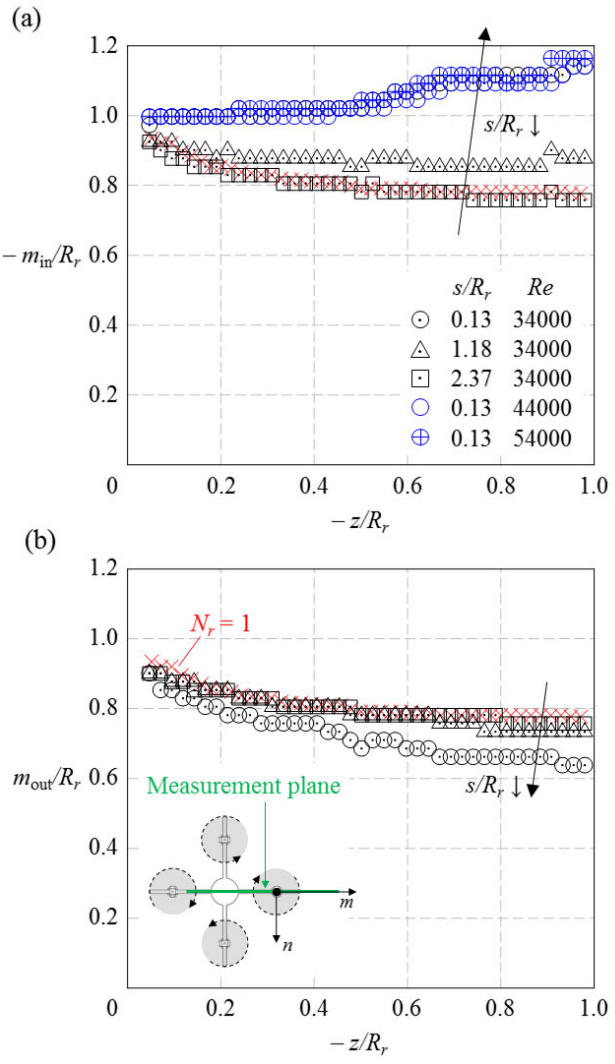


**FIGURE 13.** Variations in the (a) inner and (b) outer wake boundaries below the rotor 1 with the normalized rotor separation distance for $N_r = 4$. Wake boundary for $N_r = 1$ is also shown for comparison as red crosses. The gray circle in the inset of Fig. 13(b) indicates the area swept by the rotor blades rotating in the direction of the dashed arrow.

number of rotating rotors, in this section, we introduce a new model to predict the wake geometry of the quadrotor UAV model in hovering flight, as a function of $s/R_r$.

For a single hovering helicopter rotor with two untwisted blades, Landgrebe [7] suggested the following equation for the wake boundary:

$$r_1/R_r = A + (1 - A)\exp\left[f(\sigma, C_{T,1}, z/R_r)\right] \quad (1)$$

where

$$f(\sigma, C_{T,1}, z/R_r) = [f_{\rm I}(\sigma)/C_{T,1} + f_{\rm II}(\sigma)]z/R_r \quad \text{for } -0.25C_{T,1}/\sigma \le z/R_r \le 0 \quad (2)$$

$$= [f_{\rm III}(\sigma)C_{T,1}^{1/2} + C_{T,1}^{-1/2}z/R_r - \pi](27C_{T,1} + 0.145) \quad \text{for } z/R_r < -0.25C_{T,1}/\sigma \quad (3)$$

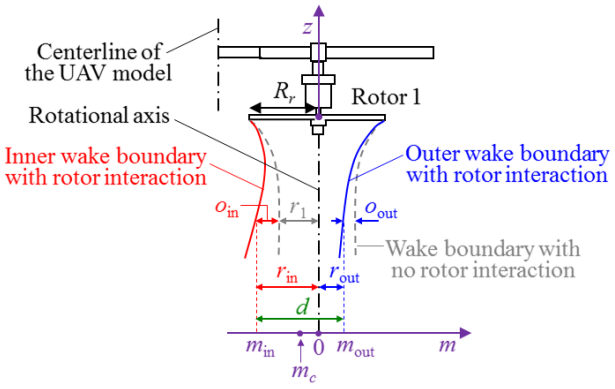


**FIGURE 14.** Modeling of the inner and outer wake boundaries with rotor interaction. Here, $d$ is the wake diameter, $o$ is the wake-boundary offset, $r_1$ is the wake radius for $N_r = 1$, and the subscripts in and out denote the quantities associated with the inner and outer wake boundaries, respectively. $m_c$ is the $m$-coordinate of the wake center, defined as the mean of $m_{in}$ and $m_{out}$.

Here, $A(= 0.78)$ is the wake contraction ratio, $r_1$ is the wake radius for a single rotor (i.e., $N_r = 1$), and $f_{\rm I}, f_{\rm II}$, and $f_{\rm III}$ are defined empirically as functions of the rotor solidity $\sigma$. As shown above, Landgrebe [7] modeled the wake geometry of a helicopter rotor by two different equations because, in his experiments, the tip vortex trailed from a model rotor blade moved axially (i.e., in the $z$-direction) with two different velocities, depending on $z/R_r$. However, for a low Reynolds number ($Re = 40900$) rotor in hover, Hein and Chopra [25] showed that the axial velocity of the tip vortex was nearly constant irrespective of $z/R_r$. This is indeed observed in our experiments (not shown here), and thus, (1) combined with (2) is used as the basis of the wake modeling. Given that the rotor solidity in this study is fixed and $C_{T,1}$ remains nearly constant in the rotational speed (i.e., Reynolds number) range investigated, (1) combined with (2) can be simplified as follows:

$$r_1/R_r = A + (1 - A)\exp[kz/R_r] \quad (4)$$

Here, $k$ is an experimental constant indicating how fast the wake of the single isolated rotor contracts, and in this study it is called the wake contraction gradient. A higher $k$ means that the rotor wake contracts faster (i.e., the diameter of rotor wake decreases more rapidly) as the wake develops downstream and vice versa. In this study, the wake contraction gradient was calculated by fitting the data in Fig. 7 to (4) and was found to be 5.16.

As was described in Sections IV-A.3 and IV-A.4, the rotor wake interaction causes the wake boundary to deviate from that for $N_r = 1$ (i.e., with no rotor interaction). Therefore, let us introduce the concept of the "wake-boundary offset ($o$)," which is defined as the distance between the wake boundary with and without the rotor interaction at a given $z$ (see Fig. 14). Considering that the inner and outer wake boundaries deviate in the direction away from and closer to the rotational axis, respectively, by the rotor wake interaction, the inner and outer wake radii can be expressed as

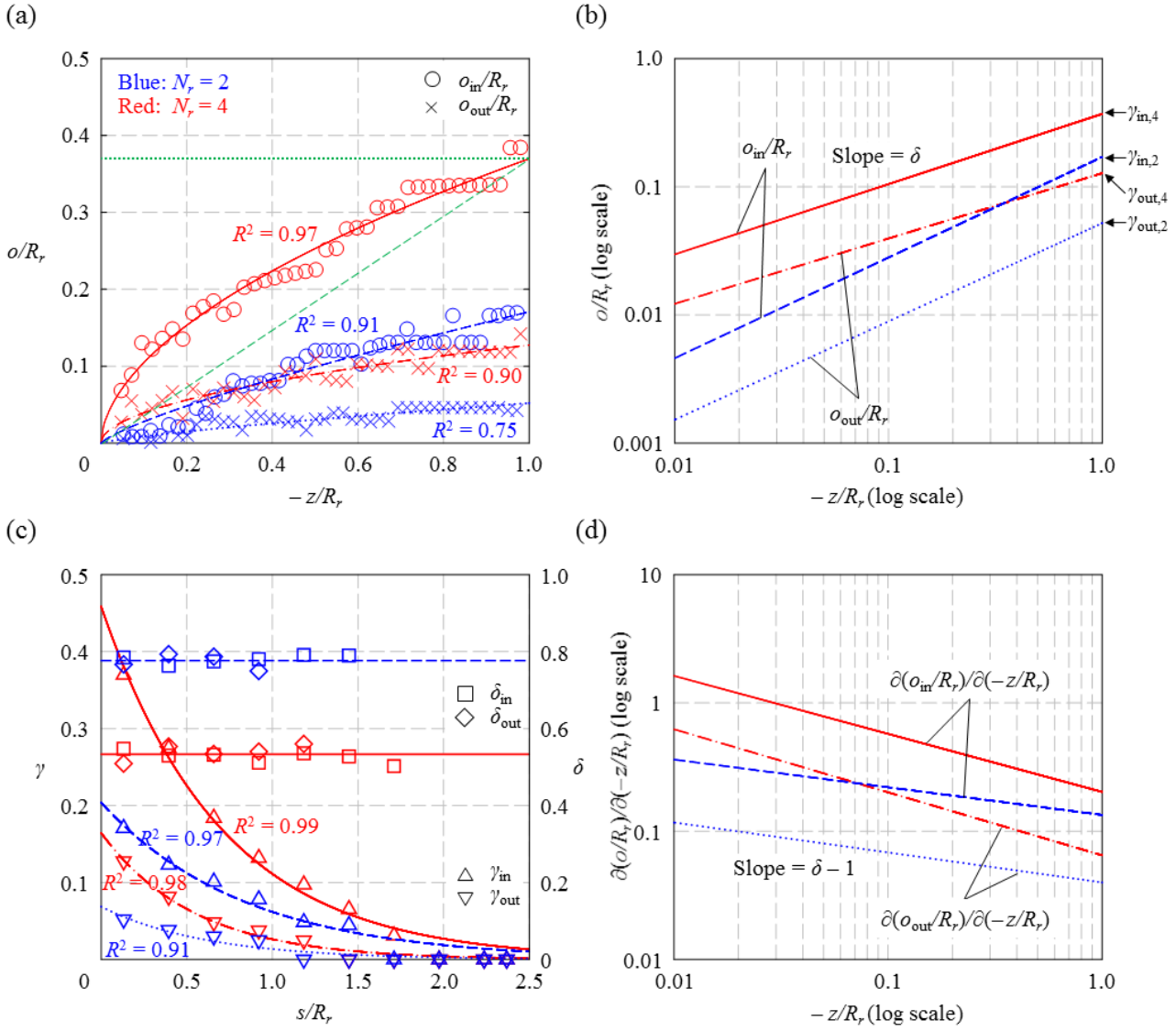


**FIGURE 15.** (a) Variations in the normalized wake-boundary offset $o/R_r$ of the rotor 1 with $z/R_r$ at $s/R_r = 0.13$ for $N_r = 2$ and 4. The curves are obtained from the best fit using (6) with the following coefficients: $\gamma_{in,2} = 0.171$ and $\delta_{in,2} = 0.785$ (blue dashed); $\gamma_{out,2} = 0.052$ and $\delta_{out,2} = 0.767$ (blue dotted); $\gamma_{in,4} = 0.370$ and $\delta_{in,4} = 0.548$ (red solid); $\gamma_{out,4} = 0.128$ and $\delta_{out,4} = 0.509$ (red dashed-dot). (b) Variations of the normalized wake-boundary offset modeled by (6) with $z/R_r$ in log-log scale. (c) Variations of $\gamma$ and $\delta$ with the normalized rotor separation distance for $N_r = 2$ and 4. The curves are obtained from the best fit using (7) with the following coefficients: $a_{in,2} = 0.204$ and $b_{in,2} = 1.192$ (blue dashed); $a_{out,2} = 0.069$ and $b_{out,2} = 1.619$ (blue dotted); $a_{in,4} = 0.459$ and $b_{in,4} = 1.417$ (red solid); $a_{out,4} = 0.165$ and $b_{out,4} = 1.835$ (red dashed-dot). (d) Variations in the streamwise gradient of the normalized wake-boundary offset with $z/R_r$ at $s/R_r = 0.13$ for $N_r = 2$ and 4.

$r_{in} = r_1 + o_{in}$ and $r_{out} = r_1 - o_{out}$, respectively. As the $m$-coordinates of the inner ($m_{in}$) and outer ($m_{out}$) wake boundaries are equals to $-r_{in}$ and $r_{out}$, respectively, the equations of the inner and outer wake boundaries can be represented in the $mz$-plane as follows, respectively:

$$-m_{in}/R_r = A + (1 - A)\exp[kz/R_r] + o_{in}/R_r \quad \text{and}$$
$$m_{out}/R_r = A + (1 - A)\exp[kz/R_r] - o_{out}/R_r \qquad (5)$$

Equation (5) is derived based on the Landgrebe's model [7], and thus will be referred to as the modified Landgrebe's model hereafter. The extent to which the inner and outer wake boundaries with the rotor wake interaction deviates from the wake boundary with no rotor wake interaction varies with $z/R_r$ depending on the normalized rotor separation distance (see Figs. 10 and 13), and thus the normalized wake-boundary offset should be a function of $z/R_r$ and $s/R_r$. As a first step in modeling the relationship between $o/R_r$ and $z/R_r$, the variations of the normalized wake-boundary offset with $z/R_r$ are plotted in Fig. 15(a) when the rotor wake interaction considered is maximum for each $N_r$. As discussed in Section IV-A.3, the tip vortex originates from the tip of the blade, and thus the one end of the wake boundary is fixed at the rotor tip, from which the boundary condition of $o/R_r$ $(z/R_r \rightarrow 0) \rightarrow 0$ can be extracted. Based on this boundary

condition, the normalized wake-boundary offset is well fitted by the following equation which will be referred to as the wake-boundary offset power law (see Fig. 15(a)):

$$o/R_r = \gamma(-z/R_r)^{\delta} \tag{6}$$

The normalized wake-boundary offset modeled by the above power law is plotted in log-log scale in Fig. 15(b) to emphasize the power law behavior. Here, $\gamma$ is the normalized wake-boundary offset at $z/R_r = -1$ (see the arrows) and is called the constant of wake-boundary offset in this paper. Higher $\gamma$ indicates that the wake boundary deviates more at the same $z/R_r = -1$. The exponent of the power law, $\delta$, is equal to the slope of the lines (in log-log space) in Fig. 15(b). As can be seen from (6), in linear-linear space, $\delta = 0$ means that the normalized wake-boundary offset is constant as $\gamma$ (i.e., horizontal line connecting two points ($z/R_r = 0$, $o/R_r = \gamma$) and ($z/R_r = -1$, $o/R_r = \gamma$); e.g., green dotted line in Fig. 15(a) for $o_{\text{in},4}/R_r$), and $\delta = 1$ means that the normalized wake-boundary offset linearly increases with decreasing $z/R_r$ (i.e., linear line connecting two points ($z/R_r = 0$, $o/R_r = 0$) and ($z/R_r = -1$, $o/R_r = \gamma$); e.g., green dashed line in Fig. 15(a) for $o_{\text{in},4}/R_r$). In Fig. 15(a), $o_{\text{in},4}/R_r$ is fitted to (6) with $0 < \delta_{\text{in},4} = 0.548 < 1$, and thus increases from ($z/R_r = 0$, $o/R_r = 0$) to ($z/R_r = -1$, $o/R_r = \gamma_{\text{in},4}$) in between the green dotted line and the green dashed line. As described above, $\delta$ determines the shape of the distribution of $o/R_r$ with respect to $z/R_r$, and thus will be referred to as the shape factor of the wake-boundary offset.

As the normalized wake-boundary offset is a function of $z/R_r$ and $s/R_r$, $\gamma$ and/or $\delta$ in (6) should be a function of the normalized rotor separation distance. To find the relationship between $\gamma$ and $s/R_r$ and between $\delta$ and $s/R_r$, the fitting procedure described above is repeated at different normalized rotor separation distances. Fig. 15(c) shows the variations of $\gamma$ and $\delta$ with the normalized rotor separation distance for $N_r = 2$ and 4. It is clearly shown that, as discussed in Sections IV-A.3 and IV-A.4, the constant of inner wake-boundary offset, $\gamma_{\text{in}}$, is larger than the constant of outer wake-boundary offset, $\gamma_{\text{out}}$, for the same number of rotating rotors. For each of the inner and outer wake boundaries, $\gamma$ is larger for $N_r = 4$ than for $N_r = 2$. As the normalized rotor separation distance increases, the rotor-rotor interaction will be weakened, and accordingly the constant of wake-boundary offset will converge to zero for both the inner and outer wake boundaries. Based on this boundary condition, $\gamma_{\text{in}}$ and $\gamma_{\text{out}}$ can be fitted by the following exponential decay function (see Fig. 15(c)):

$$\gamma = a \exp\left[-b(s/R_r)\right] \tag{7}$$

Note that in Fig. 15(c), the measured $\gamma$ is taken as zero for $s/R_r$s at which the maximum wake-boundary offset is smaller than the spatial resolution of DPIV measurements. As shown in Fig. 15(c), the shape factor of the wake-boundary offset can be fitted as $\delta_{\text{in}} = \delta_{\text{out}} = 0.776$ for $N_r = 2$ and $\delta_{\text{in}} = \delta_{\text{out}} = 0.533$ for $N_r = 4$, respectively, where $\delta_{\text{in}}$ and $\delta_{\text{out}}$ are the shape factor of the inner and outer wake-boundary offsets, respectively. It is interesting that at the same $N_r$, $\delta_{\text{in}}$, and $\delta_{\text{out}}$ remain almost constant regardless of the normalized rotor separation distance and are nearly equal to each other. Assuming that $\delta_{\text{in}} \approx \delta_{\text{out}}$ at the same $N_r$, the ratio of $o_{\text{in}}/R_r$ to $o_{\text{out}}/R_r$ can be expressed as follows using (6) and (7):

$$\frac{o_{\text{in}}/R_r}{o_{\text{out}}/R_r} = \frac{\gamma_{\text{in}}}{\gamma_{\text{out}}} = \text{constant at a given } N_r \text{ and a given} s/R_r \tag{8}$$

Equation (8) indicates that the inner wake-boundary offset is linearly proportional to the outer one at the same $z/R_r$. That is, the shape of the streamwise distribution (i.e., the distribution with respect to $z/R_r$) of the inner and outer wake-boundary offsets are geometrically similar to each other (e.g., compare the blue dashed line and the blue dotted line and the red solid line and the red dashed-dot line in Fig. 15(a)).

Equation (6) can be useful to estimate how rapidly the wake-boundary offset changes as the rotor wake convects downstream. Fig. 15(d) shows the streamwise gradient of the wake-boundary offset as a function of $z/R_r$, which is obtained by differentiating (6). From Figs. 15(b) and 15(d), it is clear that as $z/R_r$ increases (i.e., closer to the rotor-tip path plane), the wake-boundary offset decreases but the streamwise gradient of the wake-boundary offset increases for both inner and outer wake boundaries at a given $N_r$. The above discussion shows that the modified Landgrebe's model suggested in this paper can be used to systematically explore the influence of the rotor wake interaction (i.e., the number of rotating rotors and the normalized rotor separation distance) on the wake geometry of the quadrotor UAV model.

Fig. 16(a) shows the inner and outer wake boundaries of the rotor 1 in the absence of rotor wake interaction ($N_r = 1$), along with the curves obtained by the Landgrebe's model [7] and the modified Landgrebe's model. The modified Landgrebe's model (red and blue solid curves for the inner and outer wake boundaries, respectively) can describe the wake geometry better than the Landgrebe's model [7] (black dashed curve in Fig. 16(a)), giving higher coefficients of determination ($0.96 \leq R^2 \leq 0.97$) than those of the Landgrebe's model [7] ($-0.71 \leq R^2 \leq -0.56$). Note that the negative $R^2$ of the Landgrebe's model [7] implies that the model has lower predictive performance that the mean value. In the presence of strong rotor-rotor interaction (see Figs. 16(b) and 16(c)), the modified Landgrebe's model can also describe both the inner (lower panels) and outer (upper panels) wake boundaries with sufficient accuracy ($R^2 \geq 0.75$ and $R^2 \geq 0.95$ for inner and outer wake boundaries, respectively), suggesting that this model would be useful in predicting the change of wake boundary with the number of rotating rotors and the normalized rotor separation distance. Note that $R^2$ is relatively low when the wake boundary is similar to a horizontal line (e.g., $m_{\text{in}}/R_r$ at $s/R_r = 0.39$ in Fig. 16(b)) because the predictive performance of the mean value is relatively high.

Based on the modified Landgrebe's model, the effect of rotor-rotor interaction on the wake contraction can be

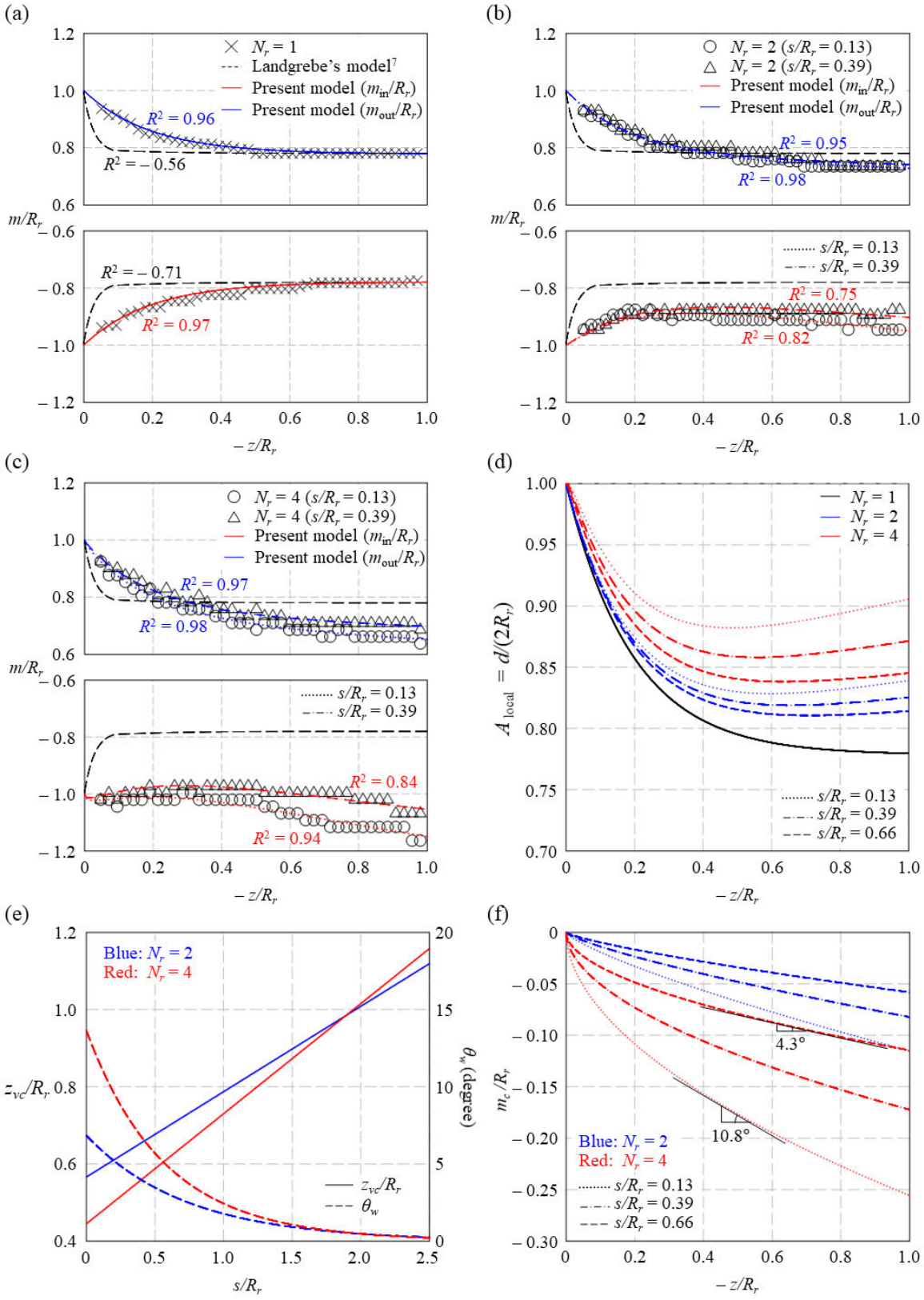


**FIGURE 16.** (a-c) Inner (lower panel) and outer (upper panel) wake boundary below the rotor 1 for (a) $N_r = 1$, (b) 2, and (c) 4. The black dashed curve corresponds to the wake boundary obtained from the Landgrebe's model [7]. (d) Variations in the local wake contraction ratio $A_{local}$ with $z/R_r$ for $N_r = 1$ (black), 2 (blue), and 4 (red) at $s/R_r = 0.13$, 0.39, and 0.66. (e) Variations of the normalized streamwise location of the *vena contracta* ($z_{vc}/R_r$; left axis) and the wake inclination angle ($\theta_w$; right axis) with $s/R_r$ for $N_r = 2$ (blue) and 4 (red). (f) Variations of the normalized $m$-coordinate of the wake centerline $m_c/R_r$ with $z/R_r$ for $N_r = 2$ (blue) and 4 (red) at $s/R_r = 0.13$, 0.39, and 0.66.

estimated in detail as shown below. Fig. 16(d) shows the local wake contraction ratio ($A_{\text{local}} = d/(2R_r)$) as a function of $z/R_r$ with varying $s/R_r$ and $N_r$, where $d$ ($= 2r_1 + o_{\text{in}}$–$o_{\text{out}}$; see Fig. 14) is the wake diameter. For $N_r = 1$, the local wake contraction ratio converges to 0.78 as the rotor wake develops downstream, giving a wake contraction ratio ($A_{\text{local}}$ at the *vena contracta*; i.e., the minimum $A_{\text{local}}$) of 0.78. The figure reveals that the stronger the rotor-rotor interaction (i.e., the higher the number of rotating rotors and the lower the normalized rotor separation distance), the less the wake contracts (i.e., the higher the local wake contraction ratio). This indicates that the difference between the inner and outer wake-boundary offset ($o_{\text{in}}$–$o_{\text{out}}$) increases as $N_r$ increases and $s/R_r$ decreases. It is important to note that the normalized streamwise location of the *vena contracta* ($z_{vc}/R_r$) where $A_{\text{local}}$ reaches its minimum varies depending on $s/R_r$ at a given $N_r$. For example, when $N_r = 4$, $A_{\text{local}}$ attains its minimum at $z_{vc}/R_r = 0.482$ and 0.634 for $s/R_r = 0.13$ and 0.66, respectively. The normalized streamwise location of the *vena contracta* as a function of $s/R_r$ is shown as solid lines in Fig. 16(e) (see left axis), which is obtained from the condition $\partial A_{\text{local}}/\partial(-z/R_r) = 0$. Fig. 16(e) clearly shows that the normalized streamwise location of the *vena contracta* moves toward the rotor-tip path plane ($z/R_r = 0$) with decreasing $s/R_r$ at a given $N_r$.

The modified Landgrebe's model can be further used to quantitatively describe how much the wake is inclined relative to the axial direction (i.e., $z$-direction) by the rotor-rotor interaction. Fig. 16(f) shows the variations of the normalized $m$-coordinate of the wake centerline, $m_c/R_r$, with $z/R_r$, where $m_c$ is defined as the mean of $m_{\text{in}}$ and $m_{\text{out}}$ (see Fig. 14). In this study, we define the wake inclination angle, $\theta_w$, as the angle between the $z$-axis and the line tangent to the wake centerline at the *vena contracta*. For example, when $N_r = 4$, the wake inclination angle is measured to be 10.8° at $z_{vc}/R_r = 0.482$ and 4.3° at $z_{vc}/R_r = 0.634$ for $s/R_r = 0.13$ and 0.66, respectively. The wake inclination angle as a function of $s/R_r$ is plotted as dashed lines in Fig. 16(e) (see right axis). This figure shows that the wake becomes more inclined relative to the axial direction as the rotor-rotor interaction becomes stronger.

### C. THRUST VARIATIONS

For $N_r = 1$, the thrust coefficient was nearly constant as $C_{T,1} = 0.033$ irrespective of the normalized rotor separation distance in the $Re$ range investigated. On the other hand, for $N_r = 2$ and 4, the thrust coefficients were smaller than $C_{T,1}$ and increased with the normalized rotor separation distance as follows: The symbols in Fig. 17 show the variations of the normalized loss of the thrust coefficient compared with $C_{T,1}$ ($(C_{T,1}–C_T)/C_{T,1}$; hereafter referred to as the normalized thrust coefficient loss) with $s/R_r$. At the minimum normalized rotor separation distance of $s/R_r = 0.13$, the thrust coefficients for $N_r = 2$ and 4 are lower than that for $N_r = 1$ by more than 4% and 8%, respectively. As found by previous studies [1]–[5], with increasing $s/R_r$, the extent of rotor-rotor interaction decreases and thus the normalized thrust coefficient loss also decreases for both $N_r = 2$ and 4. Note that the data for $N_r = 2$ and 4 at different Reynolds numbers collapse well.

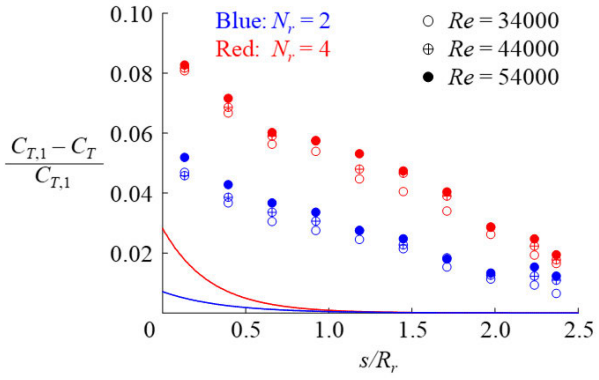


**FIGURE 17.** Variations in the normalized thrust coefficient loss with the normalized rotor separation distance. Here, the blue and red lines denote the normalized thrust coefficient loss calculated by (9) for $N_r = 2$ and 4, respectively.

According to the momentum theory, assuming one-dimensional, quasi-steady, incompressible and inviscid flow, the net force generated by a rotor is equal to the rate of change with time of the fluid momentum across the control surface enclosing the rotor disk. If the downstream control surface is placed at the *vena contracta*, considering that the rotor wake is inclined by $\theta_w$ relative to the axial direction at the *vena contracta* by the rotor-rotor interaction, the thrust force in the axial direction would be reduced by a factor of $\cos\theta_w$ as compared to that in the absence of interaction. Thus, by applying $\theta_w$ obtained with the model suggested in this work to the momentum theory, the normalized thrust coefficient loss can be expressed by the following equation:

$$\left[\frac{C_{T,1} - C_T}{C_{T,1}}\right]_{mtm} = 1 - \cos\theta_w, \tag{9}$$

where the subscript *mtm* denotes the quantity obtained from the momentum theory. The blue and red lines in Fig. 17 show the variations of $[(C_{T,1}–C_T)/C_{T,1}]_{mtm}$ with the normalized rotor separation distance for $N_r = 2$ and 4, respectively, which is calculated by applying $\theta_w$ shown in Fig. 16(e) to (9). The normalized thrust coefficient losses computed from the momentum theory are similar to the measured ones in that they increase as $N_r$ increases and $s/R_r$ decreases. However, $[(C_{T,1}–C_T)/C_{T,1}]_{mtm}$ is smaller than the measured data (symbols in Fig. 17), indicating that the momentum theory with the wake inclination angle does not fully explain the thrust loss caused by the rotor-rotor interaction.

To examine how the wake deflection is related to the thrust loss from the perspective of blade element theory, the wake boundary with maximum rotor interaction (i.e., at the minimum $s/R_r$ (= 0.13) for the maximum $N_r$(= 4)) and no rotor interaction (i.e., $N_r = 1$) is shown in Fig. 18.

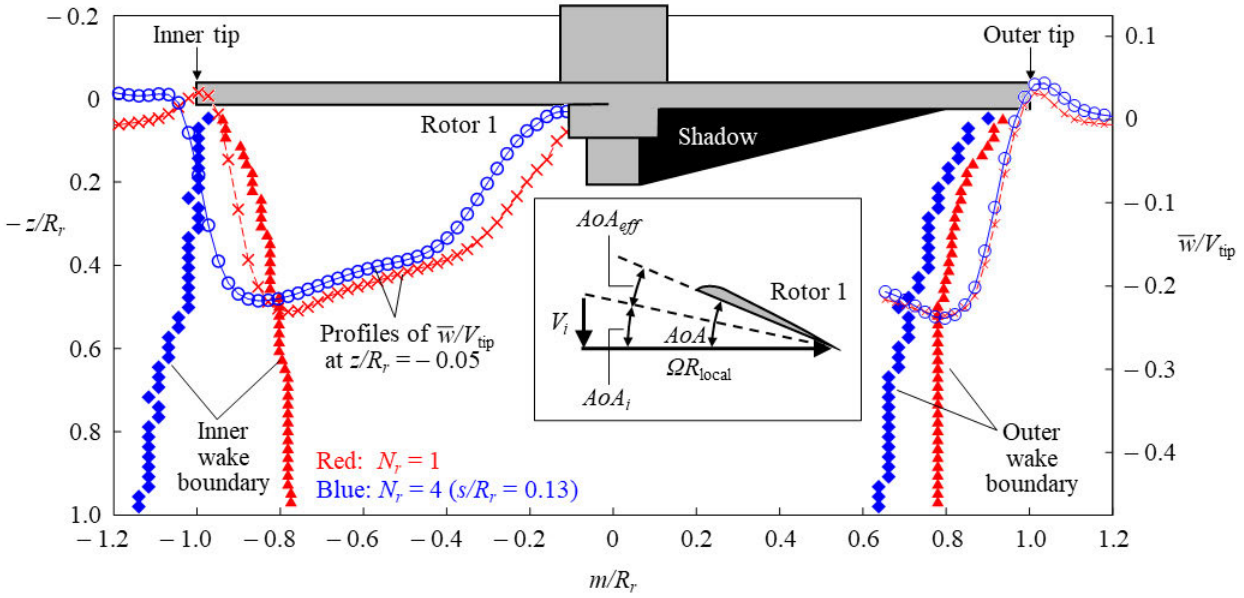


**FIGURE 18.** Wake boundaries (see left axis) and profiles of the normalized mean axial velocity $\bar{w}/V_{tip}$ at $z/R_r = -0.05$ (see right axis) for $N_r = 1$ (red) and 4 (blue). Note that some parts of the normalized mean axial velocity profiles are omitted due to the shadow cast by the UAV model. The inset shows the schematic cross-sectional view of the blade of rotor 1 representing the definition of effective angle of attack ($AoA_{eff}$). Here, $AoA$ is the geometric angle of attack, $AoA_i$ is the induced angle of attack, $V_i$ is the axial induced velocity, and $R_{local}$ denotes the local radial distance of the blade section from the rotor axis.

As the thrust is closely related to the axial induced velocity over the rotor disk, the normalized mean axial velocity profile for each case is also plotted at $z/R_r$ closest to the rotor-tip path plane (i.e., $z/R_r = 0$) in the region where the velocity is measured. It can be seen that the axial velocity profile becomes fuller near the inner tip of rotor 1 ($-1.0 < m/R_r < -0.8$) as the rotor-rotor interaction becomes stronger. This is because the tip vortex emanating from the inner tip of rotor 1 has a negative (clockwise) vorticity (see the regions represented by a dotted rectangle in Figs. 6(b) and 12(a) for $N_r = 1$ and 4, respectively), and the inner tip vortex shifts in the negative $m$-direction as the rotor-rotor interaction increases. That is, considering that the trajectory of the tip vortex is defined as the wake boundary, the deflection of the inner wake boundary away from the rotational axis would increase the axial induced velocity near the inner tip of the rotor 1. As shown in the inset, the magnitude of axial induced velocity ($V_i$) determines the induced angle of attack ($AoA_i$), and thereby determines the effective angle of attack ($AoA_{eff} = AoA - AoA_i$), where $AoA$ is the geometric angle of attack of the rotor blade. Therefore, the axial induced velocity increased by rotor-rotor interaction near the inner tip of rotor 1 would decrease the effective angle of attack by increasing the induced angle of attack, resulting in a loss of sectional thrust near the inner tip. Near the inner root of rotor 1, on the other hand, the normalized mean axial velocity is observed to decrease as $N_r$ increases from 1 to 4, which would result in an increased sectional thrust near the inner root, thereby offsetting the loss of sectional thrust near the inner tip. However, since the sectional thrust is proportional to the square of $\Omega R_{local}$, the magnitude of local thrust loss near the inner tip would exceed that of local thrust increase near the inner root, resulting in a loss of net thrust, where $R_{local}$ is the local radial distance of the blade section from the rotor axis. Contrary to the inner wake boundary, as the rotor-rotor interaction increases, the outer wake boundary is deflected closer to the rotational axis (compare two outer wake boundaries in Fig. 18). As the magnitude of wake deflection is smaller for the outer wake boundary than the inner one, the normalized mean axial velocity near the outer tip only slightly decreases with increasing the interaction strength. Note that in Fig. 18, the normalized mean axial velocity profiles are omitted between the rotational axis and $m/R_r \approx 0.64$ due to the shadow cast by the UAV model. However, from the results shown in Fig. 11(b), it can be expected that there will be no significant difference in the axial induced velocity even for the region covered by the shadow. Therefore, it can be concluded that a change in the axial induced velocity distribution accompanying the shift of the inner tip vortex and the corresponding decrease in the local effective angle of attack near the inner tip should be another important reason for the thrust loss caused by the rotor-rotor interaction.

## V. CONCLUDING REMARKS

In this paper, we have evaluated the effect of rotor-rotor interaction on the wake structure and established a model, which was referred to as the modified Landgrebe's model,

that accurately predicts the wake boundary of quadrotor UAV in hovering mode. A major improvement of the modified Landgrebe's model over the Landgrebe's model [7] is its capability of accurately predicting the asymmetric development of the wake about the rotor axis even under extremely strong mutual rotor interaction. The practical importance of the modified Landgrebe's model lies in the fact that it can be applied to improve the accuracy of the UAV-based measurement system. As the transport of gases to sensors is the critical process in various UAV-based sensing such as air quality sensing [14]–[20] and meteorological estimations [58]–[60], the wake flow generated from the UAV rotors has a considerable potential to degrade the sensor accuracy, particularly at slow or hovering flight. Therefore, in order to improve the UAV-based sensor accuracy, it is necessary to place the sensor in an optimal location that can minimize the wake influence while maintaining flight stability. Since the wake structure is essential in evaluating the effect of wake on the sensor performance, the wake geometry predicted by the model presented in this paper can provide guidance for optimizing the location of UAV-based sensors. Moreover, if the present model developed for hovering flight is extended to forward flight, it can also be used to assess the hazard of the wake of a multirotor UAV. As the wake of a leading multirotor UAV has a high potential to threaten the safety of following UAVs, the wake prediction is critical in determining the separation distance between multirotor UAVs required for flight safety [61]. In that respect, the modified Landgrebe's model, if extended to forward flight, would be a useful tool for providing essential wake information necessary to improve the flight safety of multirotor UAVs. The weakness of the modified Landgrebe's model is that the predictive value of the model is limited to the time-averaged wake geometry. However, the model can play an important role in understanding the time evolution of the rotor wake structure, such as tip vortex wandering. For example, because the principal axis of the vortex wander motion is known to be perpendicular to the mean slipstream boundary [62], [63], the wake boundary predicted by the present model would be of value in assessing the effect of rotor-rotor interaction on wandering motions of the blade tip vortex.

Using the modified Landgrebe's model suggested in this study, we have estimated the thrust loss caused by the rotor-rotor interaction from the standpoint of the momentum theory. In addition, from the perspective of the blade element theory, we have shown that the shift of the inner tip vortex away from the rotational axis and the corresponding increase of induced axial velocity followed by a decrease in the local effective angle of attack near the inner tip is another important mechanism for the thrust loss. As the momentum theory alone is insufficient to explain the loss of thrust, the correlation between the wake structure and the thrust variation presented in this paper would play a pivotal role in future research to predict the thrust loss for multirotor UAVs. Furthermore, the detailed description of how changes in the wake structure are linked to thrust generation proposed in this paper can also be applied to develop flow control strategies for minimizing the thrust loss for multirotor UAVs.

## REFERENCES

[1] W. Zhou, Z. Ning, H. Li, and H. Hu, "An experimental investigation on rotor-to-rotor interactions of small UAV propellers," in *Proc. 35th AIAA Appl. Aerodynamics Conf.*, Jun. 2017, p. 3744.
[2] H. Lee and D. J. Lee, "Rotor interactional effects on aerodynamic and noise characteristics of a small multirotor unmanned aerial vehicle," *Phys. Fluids*, vol. 32, no. 4, Apr. 2020, Art. no. 047107.
[3] S. Yoon, H. C. Lee, and T. H. Pulliam, "Computational analysis of multi-rotor flows," in *Proc. 54th AIAA Aerosp. Sci. Meeting*, Jan. 2016, p. 0812.
[4] E. J. Alvarez and A. Ning, "Modeling multirotor aerodynamic interactions through the vortex particle method," in *Proc. AIAA Aviation Forum*, Jun. 2019, p. 2827.
[5] E. J. Alvarez, A. Schenk, T. Critchfield, and A. Ning, "Rotor-on-rotor aeroacoustic interactions of multirotor in hover," presented at the Vertical Flight Soc. 76th Annu. Forum Technol. Display, Oct. 2020.
[6] D. Shukla and N. Komerath, "Multirotor drone aerodynamic interaction investigation," *Drones*, vol. 2, no. 4, p. 43, Dec. 2018.
[7] A. J. Landgrebe, "The wake geometry of a hovering helicopter rotor and its influence on rotor performance," *J. Amer. Helicopter Soc.*, vol. 17, no. 4, pp. 3–15, Oct. 1972.
[8] A. T. Conlisk, "Modern helicopter aerodynamics," *Annu. Rev. Fluid Mech.*, vol. 29, no. 1, pp. 515–567, Jan. 1997.
[9] A. T. Conlisk, "Modern helicopter rotor aerodynamics," *Prog. Aerosp. Sci.*, vol. 37, no. 5, pp. 419–476, Jul. 2001.
[10] J. G. Leishman, A. Baker, and A. Coyne, "Measurements of rotor tip vortices using three-component laser Doppler velocimetry," *J. Amer. Helicopter Soc.*, vol. 41, no. 4, pp. 342–353, Oct. 1996.
[11] J. G. Leishman, "Measurements of the aperiodic wake of a hovering rotor," *Experim. Fluids*, vol. 25, no. 4, pp. 352–361, Sep. 1998.
[12] M. Sherry, A. Nemes, D. L. Jacono, H. M. Blackburn, and J. Sheridan, "The interaction of helical tip and root vortices in a wind turbine wake," *Phys. Fluids*, vol. 25, no. 11, Nov. 2013, Art. no. 117102.
[13] T. R. Norman and J. S. Light, "Rotor tip vortex geometry measurements using the wide-field shadowgraph technique," *J. Amer. Helicopter Soc.*, vol. 32, no. 2, pp. 40–50, Apr. 1987.
[14] M. Alvarado, F. Gonzalez, A. Fletcher, and A. Doshi, "Towards the development of a low cost airborne sensing system to monitor dust particles after blasting at open-pit mine sites," *Sensors*, vol. 15, no. 8, pp. 19667–19687, Aug. 2015.
[15] C.-C. Chang, J.-L. Wang, C.-Y. Chang, M.-C. Liang, and M.-R. Lin, "Development of a multicopter-carried whole air sampling apparatus and its applications in environmental studies," *Chemosphere*, vol. 144, pp. 484–492, Feb. 2016.
[16] T. Villa, F. Gonzalez, B. Miljievic, Z. Ristovski, and L. Morawska, "An overview of small unmanned aerial vehicles for air quality measurements: Present applications and future prospectives," *Sensors*, vol. 16, no. 7, p. 1072, Jul. 2016.
[17] J. Jacob, P. Chilson, A. Houston, and S. Smith, "Considerations for atmospheric measurements with small unmanned aircraft systems," *Atmosphere*, vol. 9, no. 7, p. 252, Jul. 2018.
[18] G. Throneberry, C. M. Hocut, F. Shu, and A. Abdelkefi, "Multi-rotor wake propagation investigation for atmospheric sampling," in *Proc. AIAA Aviation Forum*, Jun. 2019, p. 3604.
[19] R. Sato, K. Tanaka, H. Ishida, S. Koguchi, J. P. R. Ramirez, H. Matsukura, and H. Ishida, "Detection of gas drifting near the ground by drone hovering over: Using airflow generated by two connected quadcopters," *Sensors*, vol. 20, no. 5, p. 1397, Mar. 2020.
[20] S. Do, M. Lee, and J.-S. Kim, "The effect of a flow field on chemical detection performance of quadrotor drone," *Sensors*, vol. 20, no. 11, p. 3262, Jun. 2020.
[21] J. Li, Y. Shi, Y. Lan, and S. Guo, "Vertical distribution and vortex structure of rotor wind field under the influence of rice canopy," *Comput. Electron. Agricult.*, vol. 159, pp. 140–146, Apr. 2019.
[22] S. Wen, J. Han, Z. Ning, Y. Lan, X. Yin, J. Zhang, and Y. Ge, "Numerical analysis and validation of spray distributions disturbed by quad-rotor drone wake at different flight speeds," *Comput. Electron. Agricult.*, vol. 166, Nov. 2019, Art. no. 105036.
[23] F. Sarghini and A. De Vivo, "Interference analysis of an heavy lift multirotor drone flow field and transported spraying system," *Chem. Eng. Trans.*, vol. 58, pp. 631–636, Jun. 2017.

[24] S. Guo, J. Li, W. Yao, Y. Zhan, Y. Li, and Y. Shi, "Distribution characteristics on droplet deposition of wind field vortex formed by multi-rotor UAV," *PLoS ONE*, vol. 14, no. 7, Jul. 2019, Art. no. e0220024.
[25] B. R. Hein and I. Chopra, "Hover performance of a micro air vehicle: Rotors at low Reynolds number," *J. Amer. Helicopter Soc.*, vol. 52, no. 3, pp. 254–262, Jul. 2007.
[26] B. Luo, Q.-H. Meng, J.-Y. Wang, and S.-G. Ma, "Simulate the aerodynamic olfactory effects of gas-sensitive UAVs: A numerical model and its parallel implementation," *Adv. Eng. Softw.*, vol. 102, pp. 123–133, Dec. 2016.
[27] T. Jing, J.-Y. Wang, and Q.-H. Meng, "An aero-olfactory-effect elimination algorithm for rotor UAV based gas distribution mapping," in *Proc. 39th Chin. Control Conf. (CCC)*, Jul. 2020, pp. 3822–3827.
[28] L. A. Young and M. R. Derby, "Rotor/wing interactions in hover," NASA, Moffett Field, CA, USA, Tech. Memo 221392, Apr. 2002.
[29] M. Veismann and M. Gharib, "High fidelity aerodynamic force estimation for multirotor crafts in free flight," in *Proc. AIAA Scitech Forum*, Jan. 2020, p. 0303.
[30] N. Intaratep, W. N. Alexander, W. J. Devenport, S. M. Grace, and A. Dropkin, "Experimental study of quadcopter acoustics and performance at static thrust conditions," in *Proc. 22nd AIAA/CEAS Aeroacoustics Conf.*, May 2016, p. 2873.
[31] J. Y. Hwang, M. K. Jung, and O. J. Kwon, "Numerical study of aerodynamic performance of a multirotor unmanned-aerial-vehicle configuration," *J. Aircr.*, vol. 52, no. 3, pp. 839–846, May 2015.
[32] J. W. Gregory, "Resolving vortex-induced pressure fluctuations on a cylinder in rotor wake using fast-responding pressure-sensitive paint," *Phys. Fluids*, vol. 31, no. 5, May 2019, Art. no. 055106.
[33] H. J. Mendes and O. Egbue, "Analysis of inverted rotors in multirotor aerial vehicles with VTOL," *IEEE Trans. Veh. Technol.*, vol. 67, no. 6, pp. 5535–5539, Jun. 2018.
[34] P. Sharma and E. Atkins, "Experimental investigation of tractor and pusher hexacopter performance," *J. Aircr.*, vol. 56, no. 5, pp. 1920–1934, Sep. 2019.
[35] C. Powers, D. Mellinger, A. Kushleyev, B. Kothmann, and V. Kumar, "Influence of aerodynamics and proximity effects in quadrotor flight," in *Proc. Int. Symp. Express Robot.*, Jun. 2012, pp. 289–302.
[36] X. Wang, S. Du, and Y. Liu, "Research on ceiling effect of quadrotor," in *Proc. IEEE 7th Annu. Int. Conf. CYBER Technol. Autom., Control, Intell. Syst. (CYBER)*, Jul. 2017, pp. 846–851.
[37] S. A. Conyers, M. J. Rutherford, and K. P. Valavanis, "An empirical evaluation of ceiling effect for small-scale rotorcraft," in *Proc. Int. Conf. Unmanned Aircr. Syst. (ICUAS)*, Jun. 2018, pp. 243–249.
[38] S. A. Conyers, M. J. Rutherford, and K. P. Valavanis, "An empirical evaluation of ground effect for small-scale rotorcraft," in *Proc. IEEE Int. Conf. Robot. Autom. (ICRA)*, May 2018, pp. 1244–1250.
[39] P. J. Sanchez-Cuevas, G. Heredia, and A. Ollero, "Experimental approach to the aerodynamic effects produced in multirotors flying close to obstacles," in *Proc. Iberian Robot. Conf.*, Nov. 2017, pp. 742–752.
[40] P. J. Sanchez-Cuevas, G. Heredia, and A. Ollero, "Multirotor aerodynamic effects in aerial manipulation," in *Aerial Robotic Manipulation*. Cham, Switzerland: Springer, Jun. 2019, pp. 67–82.
[41] J. Kim, H. Choi, H. Park, and J. Y. Yoo, "Inverse magnus effect on a rotating sphere: When and why," *J. Fluid Mech.*, vol. 754, p. R2, Sep. 2014.
[42] S.-I. Lee, J. Kim, H. Park, P. G. Jabłoński, and H. Choi, "The function of the alula in avian flight," *Sci. Rep.*, vol. 5, no. 1, p. 9914, May 2015.
[43] K. Bang, J. Kim, S.-I. Lee, and H. Choi, "Hydrodynamic role of longitudinal dorsal ridges in a leatherback turtle swimming," *Sci. Rep.*, vol. 6, no. 1, p. 34283, Oct. 2016.
[44] S. Cho, J. Kim, and H. Choi, "Control of flow around a low Reynolds number airfoil using longitudinal strips," *Phys. Rev. Fluids*, vol. 3, no. 11, Nov. 2018, Art. no. 113901.
[45] H. Kim, J. Kim, and H. Choi, "Flow structure modifications by leading-edge tubercles on a 3D wing," *Bioinspiration Biomimetics*, vol. 13, no. 6, Oct. 2018, Art. no. 066011.
[46] S. Chae, S. Lee, J. Kim, and J. H. Lee, "Adaptive-passive control of flow over a sphere for drag reduction," *Phys. Fluids*, vol. 31, no. 1, Jan. 2019, Art. no. 015107.
[47] H. Choi, J. Lee, and H. Park, "Wake structures behind a rotor with superhydrophobic-coated blades at low Reynolds number," *Phys. Fluids*, vol. 31, no. 1, Jan. 2019, Art. no. 015102.
[48] K. Taira and T. Colonius, "Three-dimensional flows around low-aspect-ratio flat-plate wings at low Reynolds numbers," *J. Fluid Mech.*, vol. 623, pp. 187–207, Mar. 2009.
[49] K. Zhang, S. Hayostek, M. Amitay, W. He, V. Theofilis, and K. Taira, "On the formation of three-dimensional separated flows over wings under tip effects," *J. Fluid Mech.*, vol. 895, p. A9, Jul. 2020.
[50] J. G. Leishman, *Principles of Helicopter Aerodynamics With CD Extra*. Cambridge, U.K.: Cambridge Univ. Press, 2006, pp. 55–114.
[51] M. Ramasamy, N. P. Gold, and M. J. Bhagwat, "Rotor hover performance and flowfield measurements with untwisted and highly-twisted blades," in *Proc. 36th Eur. Rotorcraft Forum*, Sep. 2010, pp. 770–783.
[52] Y. Lei and H. Wang, "Aerodynamic optimization of a micro quadrotor aircraft with different rotor spacings in hover," *Appl. Sci.*, vol. 10, no. 4, p. 1272, Feb. 2020.
[53] F. Caradonna, "The application of CFD to rotary wing aircraft," NASA, Moffett Field, CA, USA, Tech. Memo 102803, Mar. 1992.
[54] R. J. Fattah, W. Chen, H. Wu, Y. Wu, and X. Zhang, "Noise measurements of generic small-scale propellers," in *Proc. 25th AIAA/CEAS Aeroacoustics Conf.*, May 2019, p. 2498.
[55] J. Riou, E. Garnier, and C. Basdevant, "Compressibility effects on the vortical flow over a 65° sweep delta wing," *Phys. Fluids*, vol. 22, no. 3, Mar. 2010, Art. no. 035102.
[56] J. Sangwan, T. K. Sengupta, and P. Suchandra, "Investigation of compressibility effects on dynamic stall of pitching airfoil," *Phys. Fluids*, vol. 29, no. 7, Jul. 2017, Art. no. 076104.
[57] H. C. Ghimire and S. C. C. Bailey, "An experimental investigation of wing-tip vortex decay in turbulence," *Phys. Fluids*, vol. 29, no. 3, Mar. 2017, Art. no. 037108.
[58] P. P. Neumann and M. Bartholmai, "Real-time wind estimation on a micro unmanned aerial vehicle using its inertial measurement unit," *Sens. Actuators A, Phys.*, vol. 235, pp. 300–310, Nov. 2015.
[59] R. T. Palomaki, N. T. Rose, M. van den Bossche, T. J. Sherman, and S. F. De Wekker, "Wind estimation in the lower atmosphere using multirotor aircraft," *J. Atmos. Ocean. Tech.*, vol. 34, no. 5, pp. 1183–1191, May 2017.
[60] B. R. Greene, A. R. Segales, S. Waugh, S. Duthoit, and P. B. Chilson, "Considerations for temperature sensor placement on rotary-wing unmanned aircraft systems," *Atmos. Meas. Tech.*, vol. 11, no. 10, p. 5519, Oct. 2018.
[61] D.-G. Caprace, P. Chatelain, and G. Winckelmans, "Wakes of rotorcraft in advancing flight: A large-eddy simulation study," *Phys. Fluids*, vol. 32, no. 8, Aug. 2020, Art. no. 087107.
[62] K. Kindler, K. Mulleners, H. Richard, B. G. van der Wall, and M. Raffel, "Aperiodicity in the near field of full-scale rotor blade tip vortices," *Experim. Fluids*, vol. 50, no. 6, pp. 1601–1610, Jun. 2011.
[63] S. M. Mula, J. H. Stephenson, C. E. Tinney, and J. Sirohi, "Dynamical characteristics of the tip vortex from a four-bladed rotor in hover," *Experim. Fluids*, vol. 54, no. 10, p. 1600, Oct. 2013.

**SEUNGCHEOL LEE** received the B.S. degree in mechanical engineering from the Ulsan National Institute of Science and Technology (UNIST), Ulsan, South Korea, in 2017, where he is currently pursuing the combined M.S.-Ph.D. degree with the Fluid-Based Convergence Laboratory. His research interests include experimental fluid mechanics, rotor aerodynamics, flow control for drag reduction of bluff bodies, and noise reduction of rotor.

**SEOKBONG CHAE** received the B.S. degree in mechanical engineering from the Ulsan National Institute of Science and Technology (UNIST), Ulsan, South Korea, in 2017, where he is currently pursuing the combined M.S.-Ph.D. degree with the Fluid-Based Convergence Laboratory. His research interests include experimental fluid mechanics, bio-inspired flow control, and aerodynamic characteristics of multirotor UAV.

**SEONG YONG WOO** received the B.S. degree in automotive engineering from Kyungpook National University, South Korea, in 2009, and the M.S. degree in robotics engineering from the Daegu Gyeongbuk Institute of Science and Technology (DGIST), Daegu, South Korea, in 2016. From 2010 to 2012, he worked as an Assistant Researcher Engineer with the Technical Research Center, DCT Company Ltd. From 2016 to 2017, he worked as a Researcher with the Sensors and Aerosols Laboratory, Ulsan National Institute of Science and Technology (UNIST), Ulsan, South Korea. From 2017 to 2019, he worked as an Assistant Researcher with the Korea Institute of Robotics and Technology Convergence (KIRO) for Agricultural Robot Automation, Andong, South Korea. He is currently working as a Senior Researcher with the Institute of Andong Smart Farm (IASF), Andong. His research interests include agricultural robots, smart farm systems, and growth monitoring sensors.

**JAESUNG JANG** received the B.S. and M.S. degrees in mechanical engineering from the Pohang University of Science and Technology (POSTECH), Pohang, South Korea, in 1997 and 1999, respectively, and the Ph.D. degree in mechanical engineering from Purdue University, West Lafayette, IN, USA, in 2004. From 2004 to 2007, he worked as a Postdoctoral Research Associate for the development of cantilever biosensors for the detection of airborne viruses with the School of Electrical and Computer Engineering, Purdue University. After serving as an Assistant Professor with Chung-Ang University, Seoul, South Korea, he joined the faculty of the Department of Mechanical Engineering, Ulsan National Institute of Science and Technology (UNIST), Ulsan, South Korea, in 2010, where he is currently a Professor. His research interests include capture, manipulation, concentration, separation, and measurement of airborne particles, especially for airborne biological particles.

**JOOHA KIM** received the B.S. and Ph.D. degrees from the School of Mechanical and Aerospace Engineering, Seoul National University, Seoul, South Korea, in 2007 and 2015, respectively. After serving as a Postdoctoral Research Fellow with the Center for Turbulence and Flow Control Research, Seoul National University, he joined the faculty of the Department of Mechanical Engineering, Ulsan National Institute of Science and Technology (UNIST), Ulsan, South Korea, in 2015, where he is currently an Assistant Professor. His research interests include the low-speed aerodynamics for fixed and rotary wings and the flow control on bluff bodies.